

Effects of capillary number and flow rates on the hydrodynamics of droplet generation in T-junction microfluidic systems

Akepogu Venkateshwarlu^a, Ram Prakash Bharti^{a,*}

^aComplex Fluid Dynamics and Microfluidics (CFDM) Lab, Department of Chemical Engineering, Indian Institute of Technology Roorkee, Roorkee - 247667, Uttarakhand, INDIA

Abstract

The control and manipulation of the hydrodynamics of droplets primarily relate to flow governing and geometrical parameters. This study has explored the influences of capillary number ($10^{-4} \leq Ca_c \leq 1$) and flow rate ratio ($0.1 \leq Q_r \leq 10$) on the hydrodynamics of droplet generation in two-phase flow through T-junction cross-flow microfluidic device. The finite element method is used to solve the Eulerian framework of a mathematical model based on mass continuity, Navier-Stokes, and conservative level set equations at fixed flow ($Re_c = 0.1$). Results are presented in terms of the instantaneous phase flow field, droplet size, droplet detachment time, and generation frequency as a function of governing parameters (Ca_c and Q_r). The flow regimes namely squeezing, first transition, dripping, second transition, parallel, and jet flow are marked. In contrast to reported value of threshold $Ca_c \approx 10^{-2}$, squeezing regime exists for all Ca_c and $2 \leq Q_r \leq 10$. The flow regimes are also mapped into droplets and non-droplet zones by using threshold Ca_c which scales quadratically with Q_r . The droplet length varies linearly with Q_r in the squeezing regime. Both droplet size and frequency show a power-law relation Ca_c and Q_r in the droplet zone. Finally, predictive correlations are presented to guide the engineering and design of droplet microfluidics devices.

Keywords: Droplet microfluidics, Flow regimes, Two-phase flow, Capillary number, Interfacial effects, Droplet and Non-droplet zones

1. Introduction

The study of emulsion generation from two immiscible fluids has drawn much attention in recent years due to its versatile applications in many areas of science and engineering. For instance,

*Corresponding author.

Email address: rpbharti@iitr.ac.in (Ram Prakash Bharti)

emulsions are widely prevalent in many industrial processes and engineering fields like mixing, pumping, pharmaceuticals, cosmetics, food, agriculture, coatings and paints (Asua, 2002; Mulqueen, 2003; van der Schaaf, 2017), biomedical reagents, inks, oil recovery and mining (Barnes, 1994; Stone et al., 2004; Cristini and Tan, 2004; Whitesides, 2006; Shi et al., 2014; Mansard et al., 2016; Zhu and Wang, 2017; Gerecsei et al., 2020). The droplet generation originates from the fluid-fluid interface instability, which is attributed to the imbalance of the interfacial force between the two fluids and the inertial and viscous forces due to flow. From the Rayleigh–Plateau instability, it is understood that there is a pressure difference created between the two phases at the interface, and a combination of the additional inertial forces (i.e., momentum flux from high to low pressure) eventually leads to the detachment or breakup of the droplets (Anna, 2016). The interfacial tension acts as a gain on the interface shape divergence ($\nabla \cdot n$) and thus, increasing interfacial tension leads to more pronounced pressure gradient (as per Young-Laplace equation) and faster droplet formation. Microfluidic devices are the most useful platform to generate emulsions having uniform size droplets through various methods on a micro-scale level.

The commonly used geometries to produce different sizes of the droplets are cross-flow, co-flow, and flow-focusing microfluidic devices (Anna et al., 2003; Eggers and Villermaux, 2008; Glawdel et al., 2012a,b; Glawdel and Ren, 2012; Zhu and Wang, 2017; Doufène et al., 2019). In flow-focusing systems, due to their geometrical constraint, it is difficult to control and maintain the frequency of generation of droplets. Cross-flow (T- or cross-shaped) devices are commonly used in experimental and numerical investigations to study droplet dynamics such as formation, fission, and fusion (Li et al., 2012; Liu and Zhang, 2009; Kang et al., 2019; Liu et al., 2019) due to their distinct advantages of simple and efficiently controlled modulation of droplet size and frequency. The geometry is extensively used because of its simplicity and capability to produce mono-dispersed droplets (Zhu and Wang, 2017).

In the T-shaped microfluidic geometry, the side channel (containing a dispersed phase, DP) intersects perpendicular to the main channel (containing the continuous phase, CP) and thereby forming up a T-shape. In this arrangement, the continuous and dispersed phases, entering through inlets of the main channel and T branch, meet at the junction point and flow downstream of the

main channel along with the continuous phase (CP). Depending upon the interplay between various forces acting throughout the flow, either the two-layer flow or the emulsions consisting of droplets or bubbles of the dispersed phase (DP) may be formed. Generally, the flow through such microfluidic systems is governed by the two dimensionless numbers: capillary number ($Ca = u\mu/\sigma$) and Reynolds number ($Re = \rho uw/\mu$) representing the relative importance of viscous over interfacial forces, and inertial to viscous forces, respectively. The flow dynamics is further governed by the physical properties (density $\rho_r = \rho_d/\rho_c$, viscosity $\mu_r = \mu_d/\mu_c$) and flow rate ($Q_r = Q_d/Q_c$) of dispersed and continuous phases. Here, subscripts c , d and r denote for the continuous and dispersed phases, and ratio, respectively. Depending on the value of Ca , generally, three main regimes, i.e., dripping, jetting, and squeezing, are distinguished and reported in the literature. Smaller droplets are formed at high Ca and low Re due to stronger shearing (large viscous force) of a dispersed phase by the continuous phase. However, larger droplets are obtained at low Ca due to restricting of the downstream flow.

Many experimental and numerical studies have been conducted to understand the underlying dynamics of the droplet formation in the T-type microchannels. For instance, [Thorsen et al. \(2001\)](#) have performed experiments and reported that the geometry of channels has a significant impact on the droplet generation pattern. [Nisisako et al. \(2002\)](#) have introduced an experimental method to generate water droplets in oil in the T-junction microchannel and reported that the droplet size is inversely proportional to the flow rate of the continuous phase. [van der Graaf et al. \(2006\)](#) studied the formation of droplet necking both experimentally and numerically. Several studies have reported the influence of viscosity ratio (μ_r) on the droplet size. [Nekouei and Vanapalli \(2017\)](#) have reported that, for a fixed Ca , the droplet size increased with increasing $\mu_r > 1$ and it does not vary much for $\mu_r < 1$. At low Re , viscous and interfacial forces play a crucial role in the formation of the droplet due to insignificant inertia. At very low capillary numbers ($Ca_c \ll 10^{-2}$), the dispersed phase occupies a relatively large flow area in the main channel and resists the continuous phase stream. This leads to a higher pressure buildup in the upstream region, followed by the necking of the dispersed phase, eventually resulting in the formation of the droplet. The droplet breaks up at the junction point towards the downstream length, and it is not affected by the wall shear stress. The length of the droplet is reported to be a

function of the channel size (i.e., w_r) and the flow rate ratio (Q_r) of the two liquid phases. It has been found that the droplet length (L) varies linearly with the flow rate ratio (Q_r) (Garstecki et al., 2006) for a given microfluidic geometry. The droplets with a length (L) greater than the width (w_c) of the main channel were observed to be stable and uniform in size (Anna, 2016; Bashir et al., 2014; De menech et al., 2008; Garstecki et al., 2006). Such flow governing conditions are called a ‘squeezing regime’ and there is a transition of droplet behavior at $Ca_c \approx 10^{-2}$. For $Ca_c > 10^{-2}$, the interfacial force prevents the dispersed phase from entering into the main channel. In contrast, the inertial and viscous forces assist the same, thereby forming a droplet further downstream by the shear stresses. The droplet size decreased with increasing Ca_c . Such flow governing conditions are called the ‘dripping regime’ (Garstecki et al., 2006; Christopher et al., 2008; Bashir et al., 2011). At higher Ca_c , the flow becomes a jet-type, two-layered flow, and chaotic due to the dominance of inertial effects. Tarchichi et al. (2013) reported another flow regime, named as ‘ballon type’, at low velocities of the dispersed phase.

In general, it is challenging to generate mono-dispersed droplets due to intense competition among inertial, viscous and interfacial forces. Therefore, it is crucial to understand the droplet dynamics for a wide range of parameters. It is further acknowledged that the experimental investigations to understand of the droplet generation and underlying physics at a higher viscosity ratio ($\mu_r > 1$) for such a broad range of governing parameters become quite complex and difficult (Abate et al., 2012). Simultaneous control of the governing parameters in the experiments is another challenge (Nekouei and Vanapalli, 2017). Numerical simulations, therefore, are an alternate way to overcome the limitations encountered with the experiments to study precise simultaneous control of the flow parameters upon the droplet generation and dynamics mechanisms. For instance, a simulation study (Cristini and Tan, 2004) has shown great potential to describe the transitions accurately and capable of extending for various other geometries over a wide range of parameters.

Table 1 has summarized the relevant experimental, numerical and theoretical studies of the two-phase flow in a T-junction microfluidic devices. However, it is found that there is no single correlation known to predict whether or not there is a droplet formation for the specific values of Ca_c and Q_r .

Table 1: Summary of experimental and numerical studies of the droplet formation in a T-junction microchannel. [Num: numerical; Exp: experimental; ^aLattice Boltzmann method (LBM), ^bPhase-field method (PFM), ^cLevel set method (LSM), ^dVolume of fluid (VOF) method]

Reference	Type	Fluids	Ca_c	Re_c	w_r	Q_r	μ_r	θ°	$\sigma(mN/m)$	Remarks
Garstecki et al. (2006)	Exp	Silicone oil, water	$< 10^{-2}$	-	0.25 – 0.1	0.01 – 10	0.01 – 0.1	-	36.5	$f(Q_r, \text{geometry})$
van der Graaf et al. (2006)	Num ^a , Exp	Oil, water	$10^{-2} - 8 \times 10^{-2}$	-	1	0.05 – 1	3.44	115 – 180	1 – 15	$f(\theta, \sigma, Q_r)$
Christopher et al. (2008)	Exp	Silicone oil, water	$5 \times 10^{-3} - 0.3$	-	0.5 – 2.5	0.05 – 2.5	0.003 – 0.2	-	46	$f(\mu_r, \text{geometry})$
De menceh et al. (2008)	Num ^b	-	$10^{-3} - 7 \times 10^{-2}$	-	1	0.01 – 2	0.125 – 1	150	12.5	$f(\mu_r, \text{pressure})$
Van Steijn et al. (2010)	Exp	Fluorinated oil, water	$< 10^{-2}$	-	0.33 – 3	0.1 – 10	0.01 – 0.1	170	17.9	$f(\text{geometry})$
Bashir et al. (2011)	Num ^c , Exp	Oil, water	$10^{-3} - 10^{-2}$	0.4 – 2.4	0.6	0.05 – 0.2	0.1 – 0.8	120 – 180	1 – 10	$f(\theta, Q_r)$
Abate et al. (2012)	Exp	Oil, water	0.03 – 0.21	1	-	-	0.833	-	4	$f(\text{pressure})$
Li et al. (2012)	Num ^d	-	≤ 0.1	-	1	0.009 – 0.83	0.154	60 – 180	-	$f(\mu_r, \text{pressure})$
Shi et al. (2014)	Num ^a	-	$1.5 \times 10^{-3} - 10^{-1}$	-	0.25 – 2	0.1 – 0.9	0.25 – 1	60 – 180	-	$f(\theta, \text{geometry})$
Wehking et al. (2014)	Exp	Silicone oil, many fluids	$10^{-3} - 0.4$	-	0.5	0.084 – 49	0.01 – 1	-	5.42 – 43.12	$f(\sigma)$
Nekouei and Vanapalli (2017)	Num ^d	-	$10^{-3} - 0.5$	< 0.1	0.33 – 3	0.05 – 10	0.01 – 15	180	-	$f(\mu_r, Q_r)$
Zhang et al. (2018)	Exp	Mineral oil, water	-	-	1	0.00833 – 2	0.19 – 0.2	146.8	4	$f(\mu_r, Q_r)$
Wong et al. (2019)	Num ^c	Olive oil, water	-	-	0.4	0.04 – 0.0625	0.147 – 1	180	-	$f(\mu_r, Q_r)$
Zeng and Fu (2020)	Exp	Silicone oil, water	≤ 0.1	-	0.5 – 1.5	-	0.0125 – 0.05	-	-	$f(\mu_r)$
Present	Num ^c	-	$10^{-4} - 1$	0.1	1	0.1 – 10	0.007143 – 0.7143	135	$1.96 \times 10^4 - 1.96 \times 10^{-3}$	$f(Ca, Q_r)$ or $f(\sigma, \mu_r)$

Numerous computational fluid dynamics (CFD) approaches such as the volume of fluid (VOF) method, lattice Boltzmann method (LBM), phase field method (PFM), and level set method (LSM) are used in the literature to explore the hydrodynamics of droplets in emulsion/multiphase flows (Olsson and Kreiss, 2005; van der Graaf et al., 2006; De menech et al., 2008; Bashir et al., 2011; Li et al., 2012; Akhlaghi Amiri and Hamouda, 2013; Shi et al., 2014; Nekouei and Vanapalli, 2017; Yu et al., 2019; Wong et al., 2019). All the CFD approaches have primarily focused on tracking the topological changes of the interface in motion. Among others, LSM has shown greater accuracy and capability to capture the fluid interface (Osher and Sethian, 1988; Bashir et al., 2011) wherein the interface is represented by a level set function (ϕ). To overcome the problem of mass loss (i.e., non-conservativeness) with LSM, tuning parameters such as re-initialization or stabilization parameter (γ , m/s) and the interface thickness controlling parameter (ϵ_{ls} , m) are included to maintain the stability and speed of the re-initialization step, respectively. LSM is also known to provide accurate surface tension effect calculations (Akhlaghi Amiri and Hamouda, 2013; Olsson and Kreiss, 2005).

In summary, the above discussed literature primarily examined different regimes of the two-phase flow and droplet formation in a T-junction microfluidic systems by varying viscosity (μ_r), flow rate (Q_r), and the channel dimension ($w_r = w_d/w_c$). However, the in-depth effect of interfacial tension (σ) on the droplet generation broadly remains unexplored for a wide range of parameters (Gupta and Kumar, 2010; Glawdel et al., 2013; Wehking et al., 2014; Li et al., 2019). Further, the classification of droplet generation zones has not been thoroughly elucidated for a wide range of parameters which helps to choose a microfluidic device for a specific application. For instance, the predictive correlations are known as a function of either Ca_c or Q_r . Practically, a functional dependence of both Ca_c and Q_r needs to be considered to predict the droplet size and frequency to design a suitable microfluidic device. A thorough study of measuring droplet size and its breakup time can assist in determining the efficiency of a microfluidic device.

In the current framework, thus, a novel attempt is made to include the effect of interfacial tension (σ) between the two phases and carried out a comprehensive study for the generation and dynamics of the droplet in cross-flow microfluidic geometry for a practically wide range of flow rate (Q_r), viscosity (μ_r), and capillary number (Ca_c). The conservative level set method (CLSM)

and finite element method (FEM) based CFD approaches have been used to understand in-depth dynamics of each droplet in terms of the droplet length, frequency, formation time, and different flow regimes.

2. Physical and Mathematical Modeling

Consider the two-phase laminar flow of immiscible fluids through a T-junction cross-flow microfluidic device, as shown in Figure 1. The device consists of a main rectangular channel

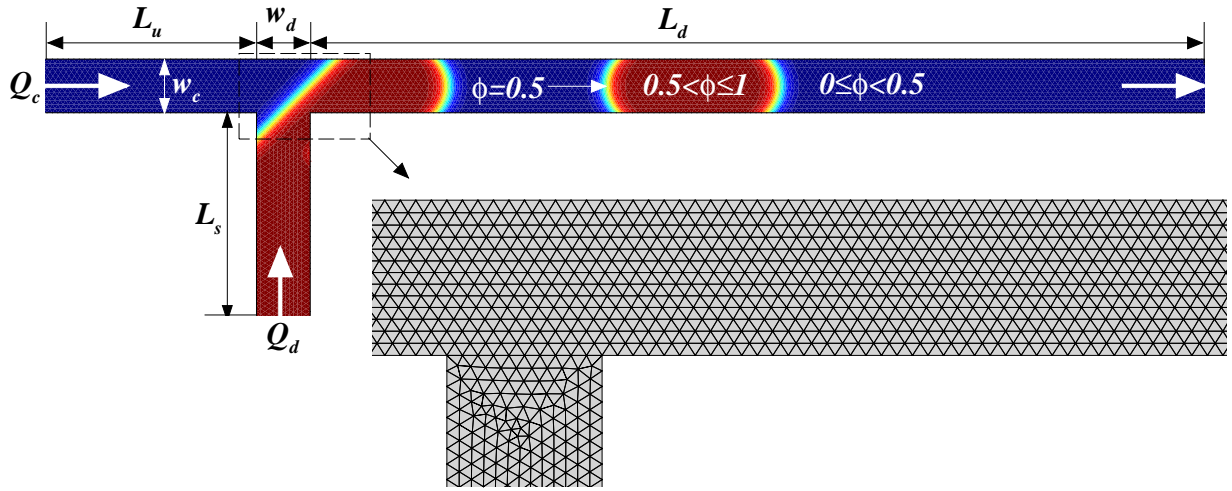


Figure 1: Schematic representation of two-dimensional T-junction microfluidic device with the triangular mesh.

(width w_c μm and length L_m μm) and a side branched channel (width w_d μm and length L_s μm). The side channel intersects perpendicular to the main channel and thereby forming up a T-junction. The branched channel is located at L_u (upstream length) and at L_d (downstream length) distances respectively from the inlet and outlet of the main channel. The length of the main channel is thus $L_m = (L_u + w_d + L_d)$.

The continuous phase (CP) and dispersed phase (DP) fluids are allowed to flow through the inlets of the main and side channels, respectively. The inlet volumetric flow rates (in $\mu\text{L/s}$) of CP and DP fluids are Q_c and Q_d , respectively. The two fluids meet at the junction point and flow downstream of the main channel along with the continuous phase (CP). The outlet of the main channel is open to ambient (i.e., outlet pressure $p = 0$). The ratios of widths of the two channels and flow rates of the two fluids are defined as $w_r = (w_d/w_c)$ and $Q_r = (Q_d/Q_c)$. Both immiscible

fluids are taken to be isothermal, incompressible and Newtonian, i.e., density, viscosity, and interfacial tension are uniform throughout the flow process.

2.1. Governing equations and boundary conditions

The flow physics under the above-noted description and approximations can mathematically be governed by mass continuity and momentum equations as follows.

$$\nabla \cdot \mathbf{u} = 0 \quad (1)$$

$$\rho(\phi) \left[\frac{\partial \mathbf{u}}{\partial t} + \mathbf{u} \cdot \nabla \mathbf{u} \right] = -\nabla p + \nabla \cdot \boldsymbol{\tau} + \mathbf{F}_\sigma \quad (2)$$

where \mathbf{u} , and p are the velocity vector, and pressure fields, respectively. The level set function (ϕ) is a smooth step function which equals to $\phi = 0$ in one fluid domain (say, CP) and $\phi = 1$ in other fluid domain (say, DP). The value of ϕ is thus ranging as $0 \leq \phi \leq 1$. Further, $\phi = 0.5$ defines the fluid-fluid interface of two-phase flow.

The deviatoric stress tensor ($\boldsymbol{\tau}$) is related with the rate of deformation tensor (\mathbf{D}) as follows.

$$\boldsymbol{\tau} = 2\mu(\phi)\mathbf{D} \quad \text{where} \quad \mathbf{D} = \frac{1}{2} \left[(\nabla \mathbf{u}) + (\nabla \mathbf{u})^T \right] \quad (3)$$

The density (ρ) and dynamic viscosity (μ) of the two-phase are expressed as follows.

$$\rho(\phi) = \rho_c + (\rho_d - \rho_c)\phi, \quad \text{and} \quad \mu(\phi) = \mu_c + (\mu_d - \mu_c)\phi, \quad (4)$$

where the subscripts 'c' and 'd' refer to the continuous and dispersed phases, respectively.

The interfacial force (\mathbf{F}_σ) between the two fluids is governed by the following relation.

$$\mathbf{F}_\sigma = \sigma \kappa \delta(\phi) \mathbf{n} \quad \text{where} \quad \mathbf{n} = \frac{\nabla \phi}{|\nabla \phi|} \quad (5)$$

where σ , \mathbf{n} , κ , and $\delta(\phi)$ are the interfacial tension (in mN/m), unit normal, the curvature of the interface, $\kappa = R^{-1} = -(\nabla \cdot \mathbf{n})$, and the Dirac Delta function, respectively.

The topological behaviour of the interface in two-phase flow can be tracked by the following

additional equation of the conservative level set method (CLSM).

$$\frac{\partial \phi}{\partial t} + \mathbf{u} \cdot \nabla \phi = \gamma \nabla \cdot [\epsilon_{ls} \nabla \phi - \phi(1 - \phi)\mathbf{n}] \quad (6)$$

The left side of Eq. (6) accounts for the motion of the interface, and the right side introduces for the necessary numerical stability. Here, \mathbf{n} is unit normal, ϵ_{ls} is the controlling parameter for thickness of region wherein ϕ goes smoothly as $0 \leq \phi \leq 1$. It is typically of the same order as that of size of mesh elements. The reinitialization or stabilization parameter (γ) ascertains the stabilization of level set function (ϕ).

The above field governing equations are subjected to the following physically realistic boundary conditions: (a) The flow rates (Q_c and Q_d) of both CP and DP are imposed at the inlets, (b) The outlet of the main channel is open to ambient, i.e., $p = 0$. Further, fully developed, i.e., Neumann condition, is imposed for the velocity and phase fields, and (c) The channel walls being solid and impermeable are subjected to the no-slip condition.

The numerical solution of the governing equations with boundary conditions results in instantaneous velocity, pressure, and phase concentration as a function of flow governing parameters. These fields are analyzed to present the droplet generation and dynamics and further used to deduce the length and diameter of the droplets. The essential definitions and parameters used in the present work are given as follows.

The effective droplet diameter (d_{eff} , m) is calculated from the surface area of the dispersed phase (Liu and Zhang, 2011; Jamalabadi et al., 2017; Wong et al., 2017, 2019) as follows.

$$d_{\text{eff}} = 2 \left[\frac{1}{\pi} \int_{\Omega} (\phi > 0.5) d\Omega \right]^{1/2} \quad (7)$$

The length of the droplet (L) is determined by plotting the phase variable (ϕ) along the length of main channel and analyzed the length occupied by $\phi > 0.5$.

The droplet detachment time (t_{dd} , s) is defined as the time interval between the two subsequent droplet formation. The droplet detachment frequency (f_{dd} , s⁻¹), i.e., the number of droplets

generated per unit time, is calculated as the inverse of the droplet detachment time.

$$t_{dd} = (t_{i+1} - t_i), \quad \text{and} \quad f_{dd} = \frac{1}{t_{dd}} \quad (8)$$

where t_i is time taken by i^{th} droplet generation (or detachment) and i is the droplet number.

The dimensionless parameters such as capillary number (Ca), Reynolds number (Re), flow rate ratio (Q_r), viscosity ratio (μ_r), density ratio (ρ_r) and channel width ratio (w_r) defined as follows.

$$\begin{aligned} Ca_c &= \frac{u_c \mu_c}{\sigma}, & Ca_d &= \frac{u_d \mu_d}{\sigma}, & Re_c &= \frac{\rho_c u_c w_c}{\mu_c}, & Re_d &= \frac{\rho_d u_d w_d}{\mu_d} & (9) \\ Ca_r &= \frac{Ca_d}{Ca_c}, & Re_r &= \frac{Re_d}{Re_c}, & Q_r &= \frac{Q_d}{Q_c}, & \mu_r &= \frac{\mu_d}{\mu_c}, & \rho_r &= \frac{\rho_d}{\rho_c}, & w_r &= \frac{w_d}{w_c} & (10) \end{aligned}$$

where, subscripts c , d and r denote for the continuous and dispersed phases, and ratio, respectively.

3. Solution Approach and Numerical Parameters

In this work, the preceding mathematical model equations based on the conservative level set method (CLSM) for two-phase laminar flow are solved using the finite element method (FEM) based COMSOL multiphysics CFD solver. The two-dimensional non-uniform linear triangular mesh has been adopted to discretize the computational domain of T-junction microfluidic device, as shown in Figure 1.

The two-dimensional (2D), laminar, two-phase flow, level set method modules of COMSOL multiphysics are used to represent the present mathematical model. The time-dependent partial differential equations (PDEs) are converted into an implicit system of ordinary differential equations (ODEs) through a finite element spatial discretization. The temporal derivatives are approximated by using the time-implicit backward differentiation formula (BDF) with variable order of accuracy from one (i.e., backward Euler method) to five. BDF method, known for their stability, is a Differential-Algebraic Equations (DAE) solver. The steps taken by solver are set to be ‘free’ with ‘automatic’ maximum time-step constraint. COMSOL selects BDF solver by default due to its stable nature for solving complex problems (Bashir et al., 2011; Sartipzadeh et al., 2020) with variable time step (Δt). It generally uses higher-order for accurate solution and selects the lower-order to obtain the stable and robust convergence.

Segregated solutions of phase (ϕ) and flow (\mathbf{u} , and p) fields are obtained by using the fastest direct solver PARDISO (PARAllel DIrect SOLver) for large sparse system of linear equations (Schenk and Gärtner, 2011; Bollhöfer et al., 2020), and Newton's non-linear solvers. The sufficiently small time step ($\Delta t = 10^{-4}$ s) is used in all the simulations. The relative tolerance of 5×10^{-3} is satisfied with the iterative solver to obtain the converged numerical solution.

The geometrical parameters for the physical system are taken as follows. Both channel widths are taken to be equal as $w_c = w_d = 100 \mu\text{m}$. The length independence test resulted the upstream and downstream lengths of main channel and the length of side branch channel as $L_u = 9w_c$ and $L_d = 30w_c$ and $L_s = 9w_c$ to be sufficient to eliminate the end effects. The values of level set parameters $\gamma=1$ m/s and $\epsilon_{ls} = h_{\text{max}}/2 = 5 \mu\text{m}$ are used in the present study, where h_{max} is the maximum size of mesh element.

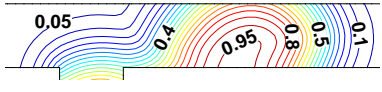
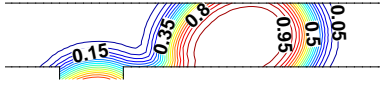
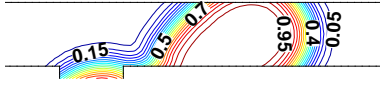
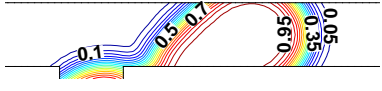
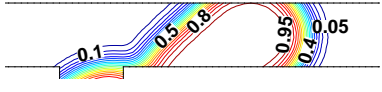
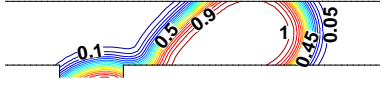
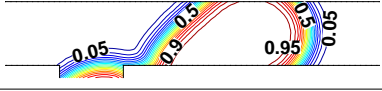
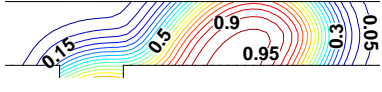
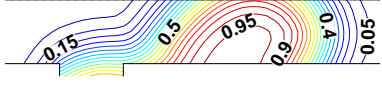
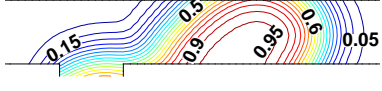
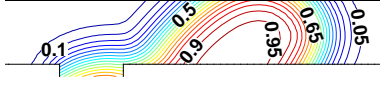
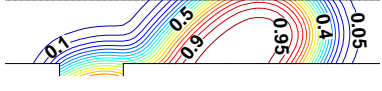
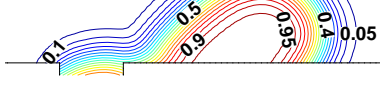
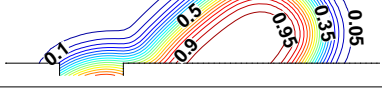
In the present study, the density of both the fluids is assumed to be equal (i.e., $\rho_r = 1$) and the contact angle (θ) with respect to the dispersed phase on the walls is taken as 135° . Further, the viscosity and the flow rate of the dispersed phase are kept constant as $\mu_d = 10^{-3}$ Pa.s and $Q_d = 0.14 \mu\text{L/s}$ (Garstecki et al., 2006; Soh et al., 2016). The numerical simulations have been performed for the ranges of conditions mentioned in Table 1 as follows. Reynolds number ($Re_c = 0.1$), capillary number ($10^{-4} \leq Ca_c \leq 1$), flow rate ($0.1 \leq Q_r \leq 10$), and viscosity ratio ($7.143 \times 10^{-3} \leq \mu_r \leq 7.143 \times 10^{-1}$), and interfacial tension ($1.96 \times 10^4 \leq \sigma \leq 1.96 \times 10^{-3}$ mN/m).

3.1. Mesh independence study

The accuracy and efficacy of the numerical solutions depend on the characteristics of the mesh used to discretize the governing equations and boundary conditions. While the solutions are expected to be most accurate when the mesh (or element) size approaches zero, the computational efforts (time and memory requirements) enhance enormously and are strongly dependent on the degree of freedom (DOF = number of nodes \times number of dependent variables). Therefore, the optimum mesh is selected through the mesh independence study by analyzing the trade-off between the accuracy of the solution and the computational efforts.

The mesh convergence analysis in Table 2 depicts the influence of triangular mesh (TM1 to TM7) size (i.e., number of mesh elements, N_e and maximum size of element, $\Delta_{\text{max}} \mu\text{m}$) on the effective droplet diameter (d_{eff} , μm), droplet detachment time (t_{dd} , ms) and evolution of the interface at a

Table 2: Data from the mesh independence study.

S.No.	Δ_{\max} (μm)	N_e	DoF	d_{eff} (μm)	t_{dd} (ms)	Evolution of the interface
(a) non-uniform triangular mesh						
TM1	13	8366	31891	168.46	22.0	
TM2	12.5	8666	33037	164.24	21.2	
TM3	11	11615	44609	163.66	21.0	
TM4	10.5	12254	47071	163.56	20.9	
TM5	10	13766	53029	163.26	20.8	
TM6	9	16409	63373	163.21	20.8	
TM7	8	20963	71697	163.20	20.8	
(b) quadrilateral mesh						
QM1	13	3814	19745	173.73	22.8	
QM2	12.5	3944	20421	172.75	22.7	
QM3	11	4933	25909	170.98	22.5	
QM4	10.5	5646	29997	170.36	22.5	
QM5	10	5910	31405	170.26	22.4	
QM6	9	6975	38199	170.13	22.3	
QM7	8	8114	43905	170.52	22.1	

fixed flow rate ($Q_r = 0.5$). Further, the structured quadrilateral meshes (QM1 to QM7) are also tested with a similar refinement in the maximum element size (Δ_{\max} , μm) from 13 to 8. Both triangular and quadrilateral meshes have shown similar consistent patterns of droplet size and breakup time, i.e., both decrease with an increasing number of elements.

Undoubtedly, the number of elements (N_e) and degree of freedom (DoF) are higher for triangular mesh in comparison to that for the quadrilateral mesh structure. For instance, $N_e = 13766$ with DoF = 53029 are in TM5 mesh whereas $N_e = 5910$ and DoF = 31045 are in QM5 mesh for $\Delta_{\max} = 10m$. Hence, the effective droplet diameter is a little bigger (and less accurate) for the quadrilateral and smaller (and more accurate) for the triangular mesh. The interface evolution and demarcation are also smooth and clear with triangular meshes compared to the quadrilateral meshes.

The analysis shows that the droplet behaviour (evolution of the interface, diameter, and detachment time) becomes strongly stable with increasing $N_e > 12254$ (i.e., refinement after TM4). The changes in the results with further mesh refinement are insignificant for $\Delta_{\max} < 10$, hence, TM5 mesh is enough to carry out the simulations. Further, DoF enhances proportionally with N_e , and so the computational efforts. Keeping in mind a trade-off between the accuracy and computational efforts, the mesh TM5 consisting of 13766 triangular non-uniform elements is considered to be sufficiently refined to resolve the gradients and interface in most accurate manner. The new results thus presented hereafter are obtained by using TM5 mesh consisting of $N_e = 13766$ non-uniform triangular elements.

4. Results and discussion

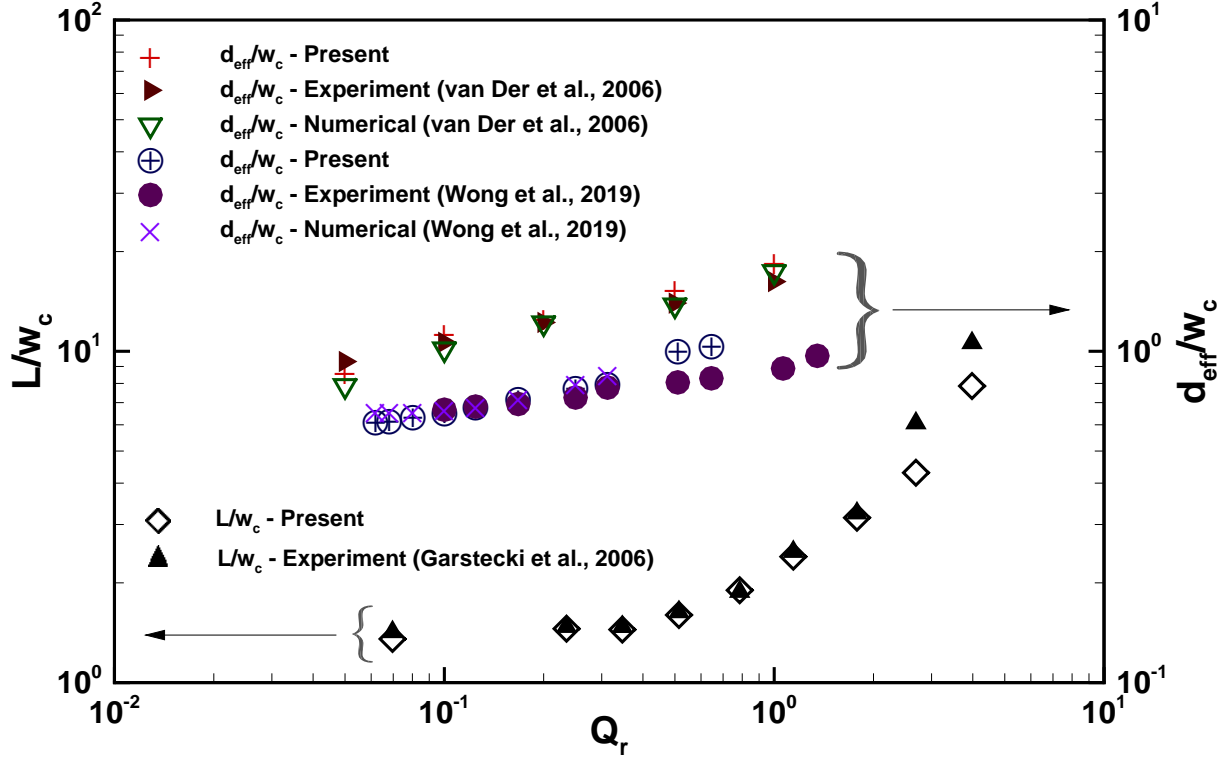
In this section, the hydrodynamics of the two-phase flow and droplet generation in T-junction microfluidic device for the wide ranges of flow governing parameters (see section 3) are presented and discussed. Before presenting the new results obtained herein, the reliability and accuracy of the solution approach are established through validation of present results with the available literature.

4.1. Validation of the results

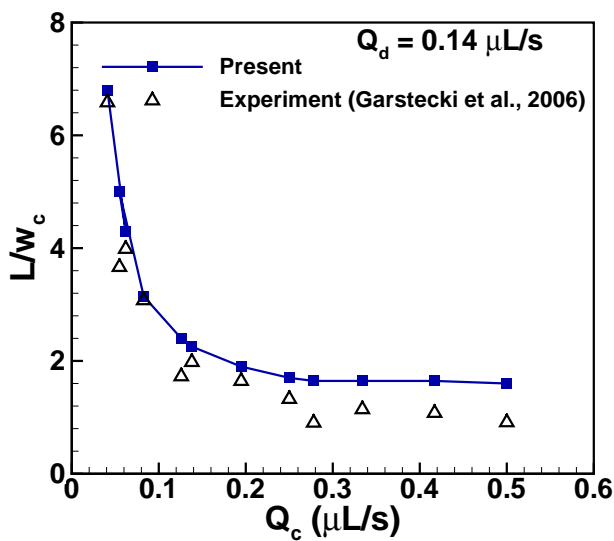
The present results in terms of the effective droplet diameter (d_{eff}) and droplet length (L) have been compared with experimental (Garstecki et al., 2006; van der Graaf et al., 2006) and numerical (van der Graaf et al., 2006; Soh et al., 2016; Wong et al., 2019) works in Figure 2. The flow and geometrical conditions are maintained consistent with the respective literature for the comparison purpose. The present values are closely consistent with the literature (Garstecki et al., 2006; van der Graaf et al., 2006; Soh et al., 2016; Wong et al., 2019) results for wide range

of flow conditions (Ca_c , Q_r , Q_c , and Q_d).

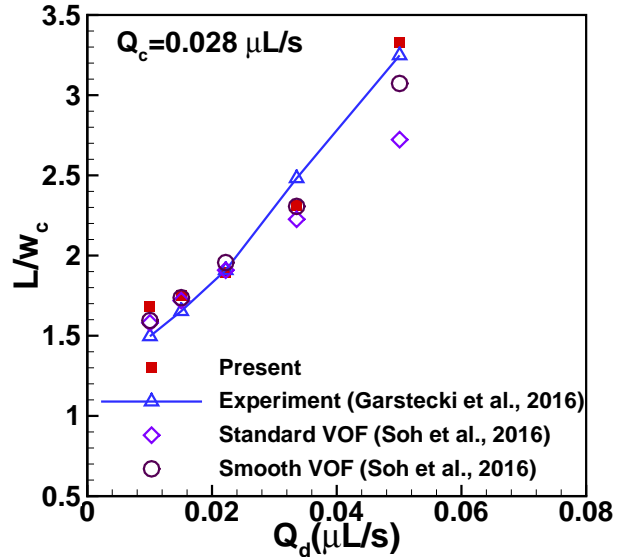
Figure 2 shows that the effective droplet diameter (d_{eff}) and droplet length (L) are decreasing with increasing flow rate of the continuous phase (Q_c) at a constant flow rate of the dispersed phase



(a) L/w_c vs. Q_r and d_{eff}/w_c vs. Q_r



(b) L/w_c vs. Q_c



(c) L/w_c vs. Q_d

Figure 2: Comparison of the present results with the literature for the wide range of $2 \times 10^{-3} \leq Ca_c \leq 4 \times 10^{-2}$ (van der Graaf et al., 2006), $Ca_c = 10^{-1}$ (Wong et al., 2019), and $Ca_c \leq 10^{-2}$ (Garstecki et al., 2006; Soh et al., 2016) and flow rate ($10^{-2} \leq Q_r \leq 10$).

(Q_d). Vice versa, L increases with increasing Q_d for fixed Q_c . Broadly, the present results are much closer to the experimental results than the numerical results obtained by using the lattice Boltzmann method (LBM) with adopted interface tracking method (van der Graaf et al., 2006), the level set method (Wong et al., 2019) and VOF (Soh et al., 2016). It is because of the comparatively finer mesh used in the present work than that used by other numerical studies (van der Graaf et al., 2006; Soh et al., 2016; Wong et al., 2019).

Based on our previous experience of CFD simulations of various problems (Bharti et al., 2006; Sivakumar et al., 2006; Bharti et al., 2007a,b; Patnana et al., 2009, 2010; Tian et al., 2014; Ram et al., 2016; Gangawane and Bharti, 2018; Kumar et al., 2021; Vishal et al., 2021), a slight deviation is quite common in simulation studies due to inherent characteristics of numerical solvers and methodologies used in related studies. Based on the above excellent agreement of present and literature values of d_{eff} and L for the broader range of Ca_c and Q_r , the present results are believed to have an excellent level ($\pm 1\%$) of accuracy.

4.2. Instantaneous phase flow profiles

The hydrodynamics of two-phase flow and droplet generation is shown in Figures 3 and 4 through instantaneous phase (ϕ) flow profiles in a microfluidic device for a wide range of flow rate ratio ($10^{-1} \leq Q_r \leq 10$) and capillary number ($10^{-4} \leq Ca_c \leq 1$). Each flow conditions show the four stages of the flow and droplet generation as follows: (i) evolution of the dispersed phase, (ii) droplet breakup stage, (iii) stable droplet formation, and (iv) channel filled with the hydrodynamically developed droplets/dispersed phase. To highlight the instantaneous evolution of the dispersed phase, the length of channel shown in the figures is varied according to the movement of the dispersed phase in the downstream of the main channel.

Figure 3 depicts the effect of interfacial tension (Ca_c) on the phase flow behaviour for a fixed flow rate ratio (Q_r). It can be noted that, in the initial stage, when the dispersed phase enters into the main channel, the viscous and pressure forces that rise in the upstream region are sufficient to overcome the interfacial force to form a droplet. Once the hydrodynamic development of liquid phases in the channel is established, the flow becomes stratified.

Figure 3a presents a special case of equal flow rate of both the phases ($Q_r = 1$, i.e., $Q_d = Q_c$). At lower values of $Ca_c (< 10^{-2})$, the elongated droplets ($L/w_c \gg 1$) generate immediate after the

interaction of two phase. The fluid flow in such cases is primarily attributed to the dominance of the interfacial force balanced by the pressure rise in the upstream region. At $Ca_c = 2 \times 10^{-2}$, the location of droplet detachment shifts towards the downstream with an increase in time, and both the immiscible fluids flow parallel to each other. The size of subsequently generated elongated droplets ($L/w_c > 1$) also reduces. Therefore, there is a transition occurring at $Ca_{c,trans} \approx 2 \times 10^{-2}$. For $Ca_c > Ca_{c,trans}$, the strengthening of the viscous (i.e., shear) stress results in the formation of a stratified/parallel flow. Further, an increasing portion of the downstream region is occupied by the stratified flow with increasing Ca_c . It results in the reduction of the downstream region available for the droplet formation. Therefore, it is evident that the interplay between the viscous and interfacial forces has a significant impact on the droplet formation even for the simplest limiting case of $Q_r = 1$. Such flow behaviors, however, change with the flow rate ratio (Q_r), as seen in Figures 3b and 3c.

Figure 3b presents the phase (ϕ) flow profiles for $Q_r = 10$ wherein the droplet formation can be witnessed at much lower values of $Ca_c (\approx 10^{-4})$. However, two-layered stratified flow is visible

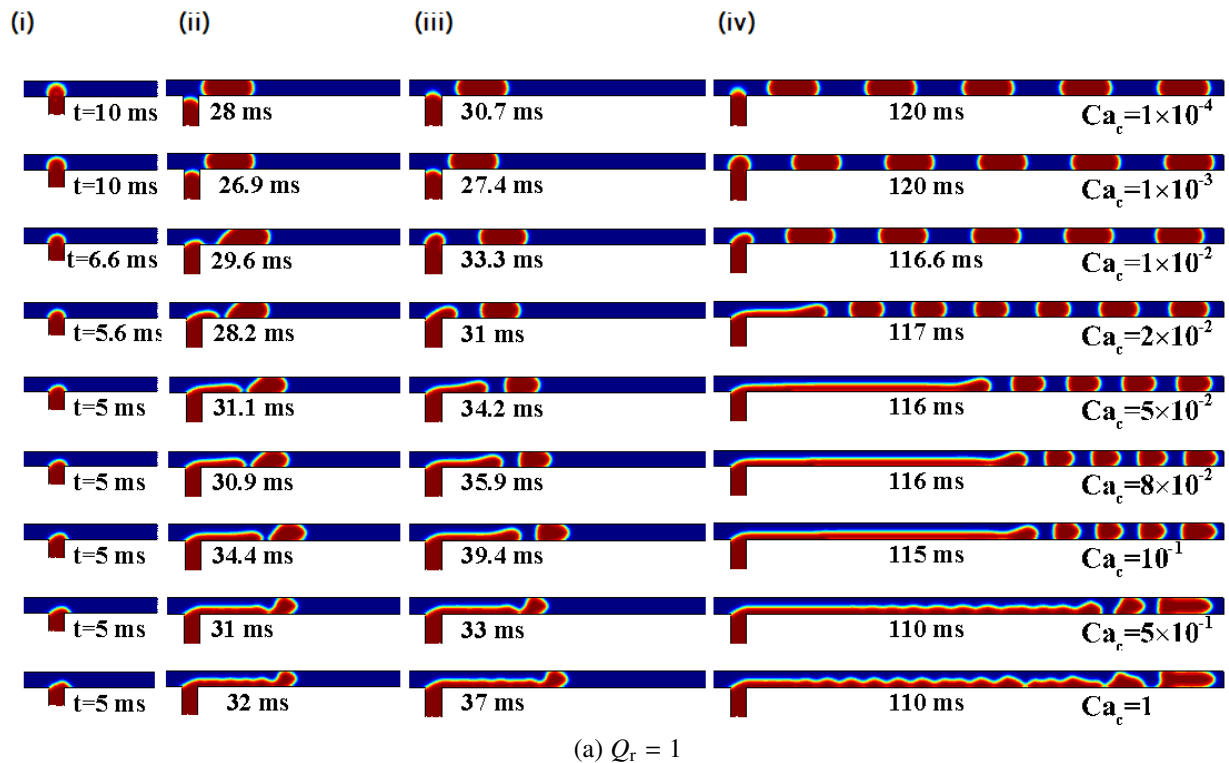
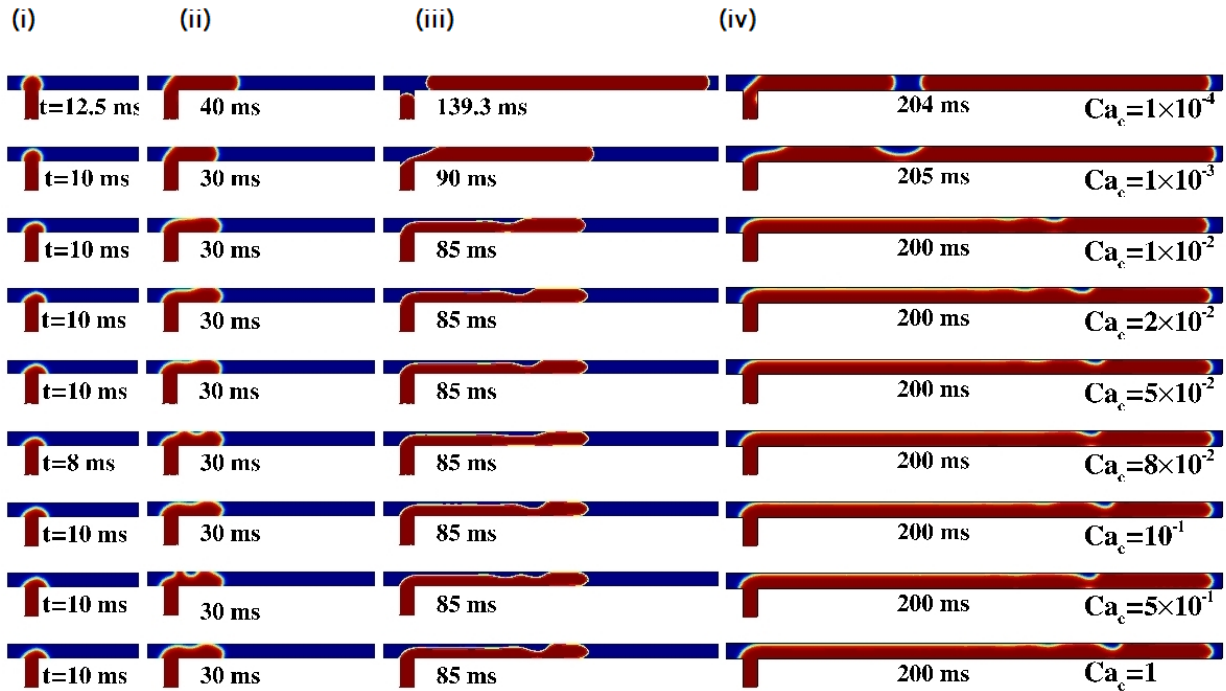
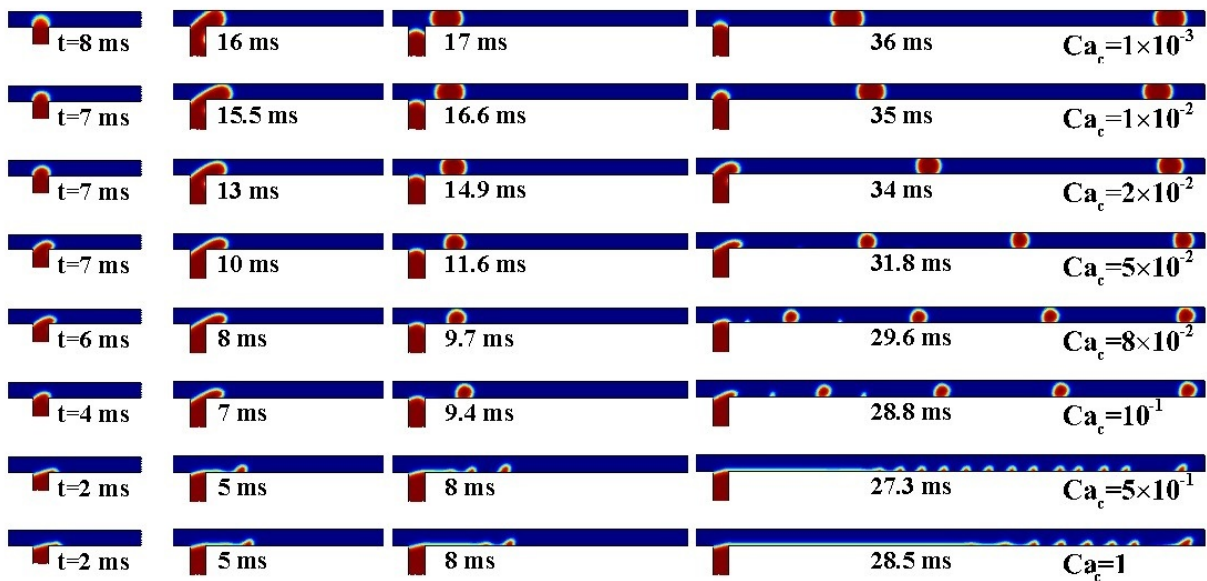


Figure 3: Instantaneous phase (ϕ) flow profiles for $10^{-4} \leq Ca_c \leq 1$. (i) evolution of the dispersed phase, (ii) droplet breakup stage, (iii) stable droplet formation, and (iv) channel filled with the hydrodynamically developed droplets/dispersed phase.

for $Ca_c > 10^{-3}$. It is reported in literature (Garstecki et al., 2006) for $Ca_c < 10^{-2}$ that majority of the downstream region is filled with the dispersed phase. It thereby causes the pressure rise in the upstream region, which is the primary contributor to provide the necessary mechanism for droplet formation. This flow nature corresponds to the ‘squeezing regime’ of two-phase flow. When $Ca_c \gtrsim 10^{-2}$, the shear stress becomes more important to initiate the droplet breakup, and the flow follows ‘dripping like regime’. Surprisingly, the present study has observed that the ‘squeezing



(b) $Q_r = 10$



(c) $Q_r = 1/10$

Figure 3: Continued.

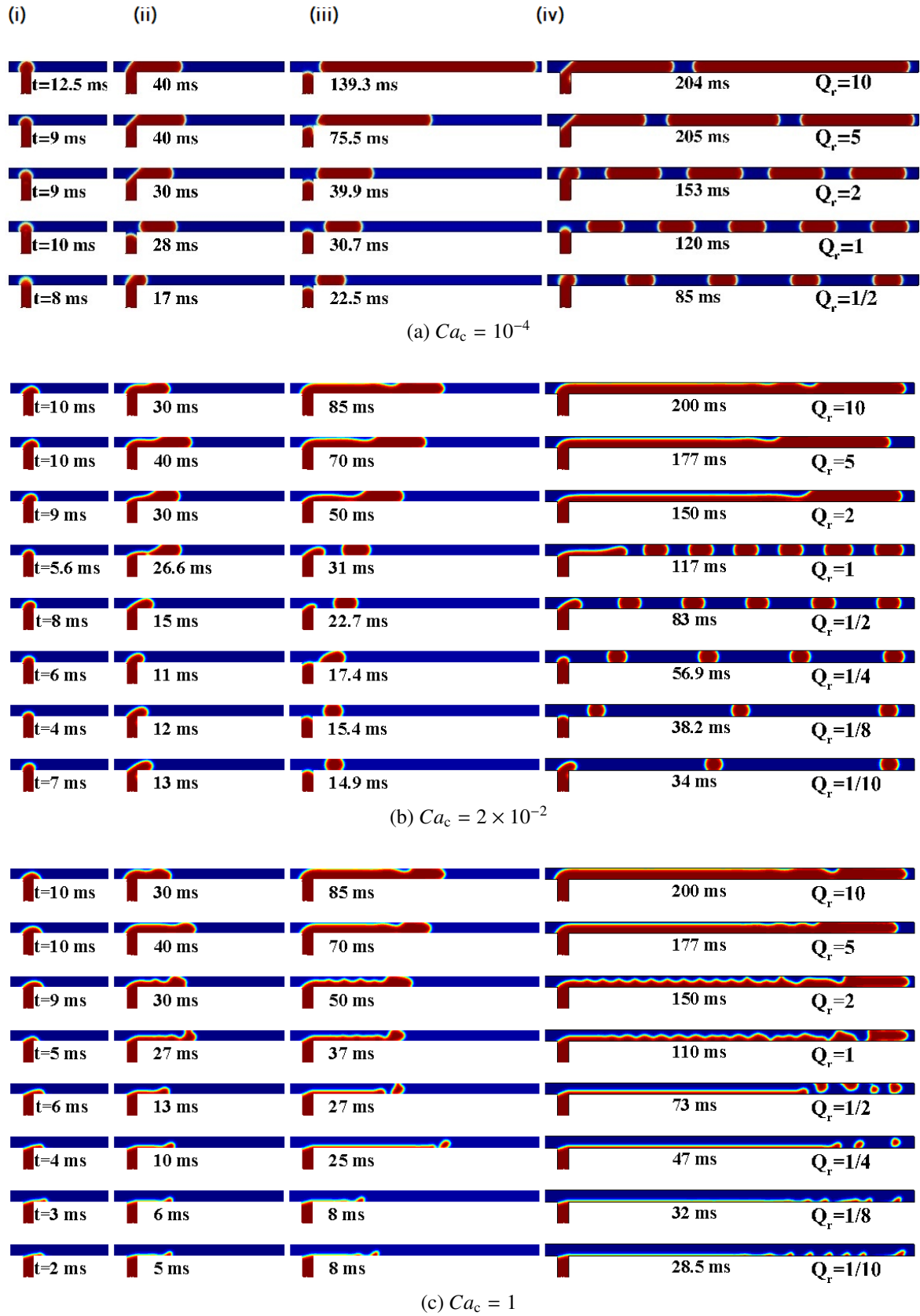


Figure 4: Instantaneous phase (ϕ) flow profiles for $10^{-1} \leq Q_r \leq 10$. (i) evolution of the dispersed phase, (ii) droplet breakup stage, (iii) stable droplet formation, and (iv) channel filled with the hydrodynamically developed droplets/dispersed phase.

regime' continues even for $Ca_c > 10^{-2}$ for a fixed $Q_r (\geq 2)$. This effect is attributed solely to the variation of interfacial tension, i.e., $Ca_{c,trans}$ value is dependent only on the surface tension for a fixed Q_r .

At the lower $Q_r (< 0.5)$, the droplets being formed are smaller in size compared to that at the higher Q_r , as shown in the phase (ϕ) flow profiles in Figure 3c for $Q_r = 0.1$. It is also noted from Figure 3c that the distance between the subsequent droplets has increased significantly. It implies that as Q_r is decreased (i.e., Q_c increased while keeping Q_d constant), the generated droplets are rapidly swept away with continuous fluid phase. Moreover, for lower $Q_r = 0.1$, the droplets are almost circular in shape with a diameter of droplet in the order of the channel width (i.e., $d_{eff} \leq w_c$).

Subsequently, combined effects of the interfacial tension and fluid viscosity on the droplet formation are analyzed through the phase (ϕ) flow profiles in Figure 4 in the range $10^{-1} \leq Q_r \leq 10$. The variation of Q_r for fixed Ca_c implies that the interfacial tension force and viscous force of the continuous phase responsible for the droplet formation are balanced, in order to maintain a constant Ca_c . Figure 4a displays the phase (ϕ) flow profiles for $5 \times 10^{-1} \leq Q_r \leq 10$ at lowest $Ca_c = 10^{-4}$. At higher $Q_r \geq 5$, the plug type (i.e., axially elongated) droplets are formed. The length of droplet is generally at least ten times higher than the channel width ($L/w_c \gtrsim 10$). On further decrease in $Q_r (\leq 2)$, the length of the droplets decreases, and eventually resulting in droplets of lengths comparable to the channel width ($L/w_c \approx 1$) for significantly low Q_r . The generated droplets are clearly distinguishable and mono-dispersed in nature. The distance between the subsequent droplets is also uniform in this region. Also, the time taken to form the droplets is decreased, and droplets generation frequency is increased on varying Q_r from 10 to 1/2.

Figure 4b presents the observations of the formation of the droplet at a relatively larger $Ca_c (= 2 \times 10^{-2})$. At higher $Q_r (\geq 2)$, droplets are not formed as the dispersed phase is flowing and occupying more volume of the downstream channel until it reaches the outlet of the channel. It is also evident that the pressure rise in the upstream and shear stress exerted by the outer fluid is not sufficient to break the interface between the two fluid phases. On varying Q_r from 1 to 1/10, the distance between the subsequent droplets is increasing as the viscosity ratio (μ_r) is decreasing,

and this trend is consistent with the observations reported in literature (Liu and Zhang, 2011). Furthermore, the phase flow behaviours shown in Figure 4c are observed for a spacial case of $Ca_c = 1$ wherein both viscous and interfacial forces contribute equally. In this case, droplet formation is not seen irrespective of Q_r . The flow is stratified and jet-type at $Q_r > 1$ and $Q_r < 1$, respectively.

In general, the two-phase flow patterns have shown a complex interplay of inertial, viscous, and interfacial forces in governing the the hydrodynamics of droplet generation. The flow patterns are categorized in the subsequent section.

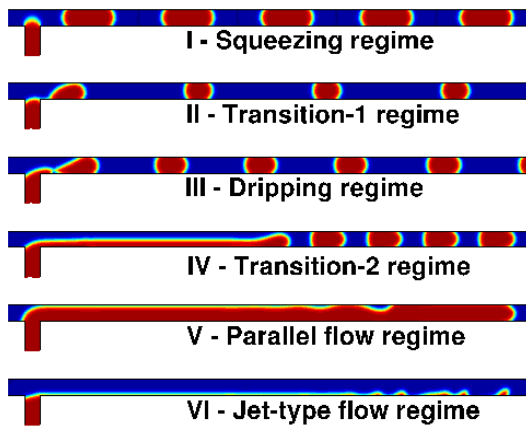
4.3. Classification of flow regimes

The phase profiles (Figures 3 and 4) have displayed that the flow patterns are strongly influenced by the flow rate (Q_r) and capillary number (Ca_c). Various transitional features are also noted under otherwise identical flow governing conditions. Figure 5a has schematically represented the nature of flow during various transitions observed for the ranges of conditions studied herein. In culmination, essentially, six types of flow regimes, namely, (I) squeezing, (II) first transition, (III) dripping, (IV) second transition, (V) parallel, and (VI) jet-type flow, are observed in the present study. The ranges of conditions for each flow regime are summarized in Figure 5b and also sketched through the flow map in Figure 5c.

The ‘squeezing regime’ is observed for the low values of $Ca_c \ll 10^{-2}$ wherein the highly elongated droplets ($L \gg w_c$) are generated. The ‘dripping regime’, wherein the low-to-negligible elongated droplets ($L \geq w_c$), is seen for $2 \times 10^{-2} < Ca_c < 10^{-1}$ and $1/2 < Q_r < 1/10$. The droplets generated in this regime are generally mono-dispersed in nature. The ‘first transition’ between the ‘squeezing’ and ‘dripping’ regimes is occurring at $Ca_c \approx 10^{-2}$ for $Q_r \leq 1$ wherein the droplet size reduces in large extent. The ‘second transitional’ regime appears in between the ‘dripping’ and ‘parallel flow’ regimes for $2 \times 10^{-2} < Ca_c < 10^{-2}$ and $1/4 \leq Q_r \leq 1$. In this regime, few droplets formed in the initial stage, immediately after the interaction of both phases in the downstream channel. Subsequently, the dispersed phase is flowing parallel to the continuous phase. The ‘parallel flow’ regime appears after the second transition for $Ca_c \leq 10^{-2}$ and $Q_r > 1$. In this type of flow, the dispersed phase enters the channel and fills the entire downstream region. After some finite time, a moving interface is eventually

created between the two immiscible phases due to the strong resistance imposed by the dispersed phase on the continuous phase. It, consequently, prevents droplet formation. Further, a ‘jet-type flow’ regime appears for $Ca_c > 10^{-2}$ and $Q_r < 1$. In this regime, the dispersed phase continues to flow, until the outlet of the main channel, as a single thread-like jet without droplet formation, due to the dominance of inertia imposed by the continuous phase. The droplet formation in the second transition, parallel and jet-type flow regimes is not affirmative.

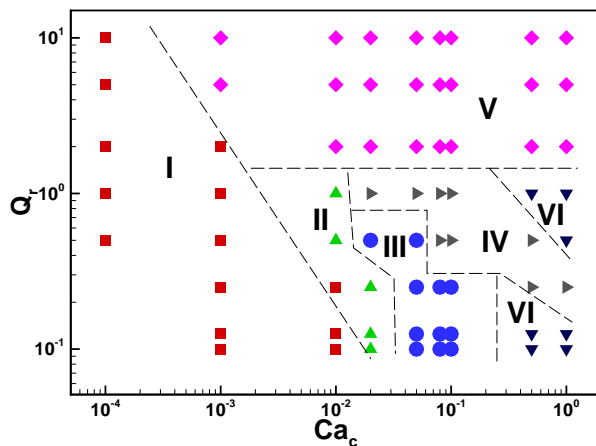
It has been established above that the droplets are certainly formed in the first three (i.e., squeezing, the first transition, and dripping) flow regimes. In contrast, droplet formation is not evident in the other three (second transition, parallel, and jet-type) flow regimes. The two-phase flow behaviour in microfluidic geometry, thus, can also be categorized into the ‘droplet’ and ‘non-droplet’ zones, as depicted in Figure 5d. These two zones are distinguished through the ratio of the threshold capillary numbers of the dispersed and continuous phases



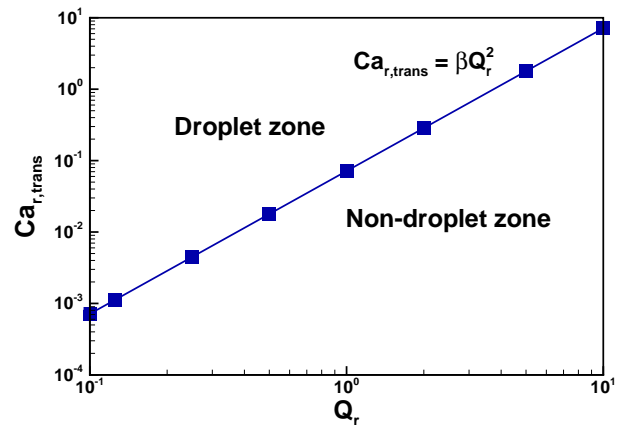
(a) Schematics of flow regimes characterization

Regime	Ca_c	Q_r	Droplets
I	$< 10^{-2}$	$0.1 \leq Q_r \leq 10$	Yes
II	$\approx 10^{-2}$	≤ 1	
III	$2 \times 10^{-2} < Ca_c < 10^{-1}$	$0.5 < Q_r < 0.1$	No
IV	$2 \times 10^{-2} < Ca_c < 10^{-2}$	$0.25 \leq Q_r \leq 1$	
V	$\leq 10^{-2}$	> 1	
VI	$> 10^{-2}$	$0.1 \leq Q_r \leq 0.125$ $0.5 \leq Q_r \leq 1$	

(b) Ranges of conditions



(c) Flow regime map



(d) Droplet and non-droplet zones

Figure 5: Classification of regimes for two-phase flow through T-junction microfluidic device.

($Ca_{r,trans} = Ca_{d,trans}/Ca_{c,trans}$). For example, the transition from the ‘droplet’ to ‘non-droplet’ zone for $Q_r = 1$ takes place (see Figure 3a) at $Ca_c = 2 \times 10^{-2}$ and correspondingly at $Ca_d = 1.43 \times 10^{-3}$, and therefore, $Ca_{r,trans} = 7.15 \times 10^{-2}$.

To depict the ‘droplet’ and ‘non-droplet’ zones in two-phase microfluidic flows, Figure 5d displays the variation of $Ca_{r,trans}$ with Q_r over the ranges of conditions explored in this work. Markedly, a log-log curve between $Ca_{r,trans}$ and Q_r separates the ‘droplet’ and ‘non-droplet’ zones by a straight line characterized by $Ca_{r,trans}$ proportional to square of Q_r , as expressed by Eq. (11).

$$Ca_{r,trans} = \beta Q_r^2 \quad \text{where} \quad Ca_{r,trans} = \frac{Ca_{d,trans}}{Ca_{c,trans}} \quad (11)$$

where $\beta = 0.07143$ is obtained by statistical analysis of the numerical data. In other words, the straight line (Eq. 11) flow map represents a boundary between zones (III) dripping and (IV) second transition. It is noted that there is a precise formation of the droplets above the curve (Figure 5d), and hence, called the ‘droplet zone’. For the combination of $Ca_{r,trans}$ and Q_r under the curve, the viscous force exerted by the continuous phase at the interface is not sufficient to overcome the interfacial tension force. Due to this, both the continuous and dispersed phases are flowing parallel to each other without any droplet formation. At very high $Ca_{r,trans}$, the dispersed phase attains a jet-type flow as the continuous phase exerts a considerable viscous force on the interface of the dispersed phase. It is thus unable to produce droplets, and called the ‘non-droplet’ zone. Further, in addition to Ca_r and Q_r , the viscosity and density of fluid phases significantly influence the hydrodynamic nature. The proportionality factor (β) demarcating the boundary between the ‘droplet’ and ‘non-droplet’ zones thus may be related to Reynolds number ratio (Re_r) of the two phases. It, however, cannot be affirmed at this stage, and more experimentation is required with varying Re_r to affirm the functional relationship between β and Re_r .

The above discussed phase (ϕ) flow profiles (Figures 3 to 5) show a complex interplay of inertial, viscous, and interfacial forces governing the hydrodynamics of two-phase flow and droplet generation in microfluidic systems. The droplet behaviour as function of Ca_c and Q_r is further analyzed in subsequent sections.

4.4. Droplet size

In order to investigate the combined influences of the interfacial tension, viscosity, and flow rate on the droplet size, Figures 6 and 7 have plotted for the length of each droplet as a function of Ca_c and Q_r . The dependence of dimensionless droplet length (L/w_c) on capillary number (Ca_c) for each sequentially generated droplets is shown in Figure 6 for the favourable conditions (Eq. 11) of droplet generation. In each plot, the flow rate ratio (Q_r) has been kept constant, whereas Ca_c is varied in order to emphasize the effect of interfacial tension on the length of each droplet.

As the phase flow profiles (Figures 3 to 4) have displayed shrinkage of droplets with increasing Ca_c , the length of droplets (L/w_c) is inversely proportional to Ca_c . At higher $Q_r > 1$ and lower $Ca_c < 10^{-2}$, the elongated droplets, like plug type, are formed wherein $L/w_c \gg 1$. All the subsequent droplets generated are found to exhibit almost the same length as that of the first droplet for a given Q_r and Ca_c . This observation also holds for low Q_r when $Ca_c < 10^{-2}$, as seen

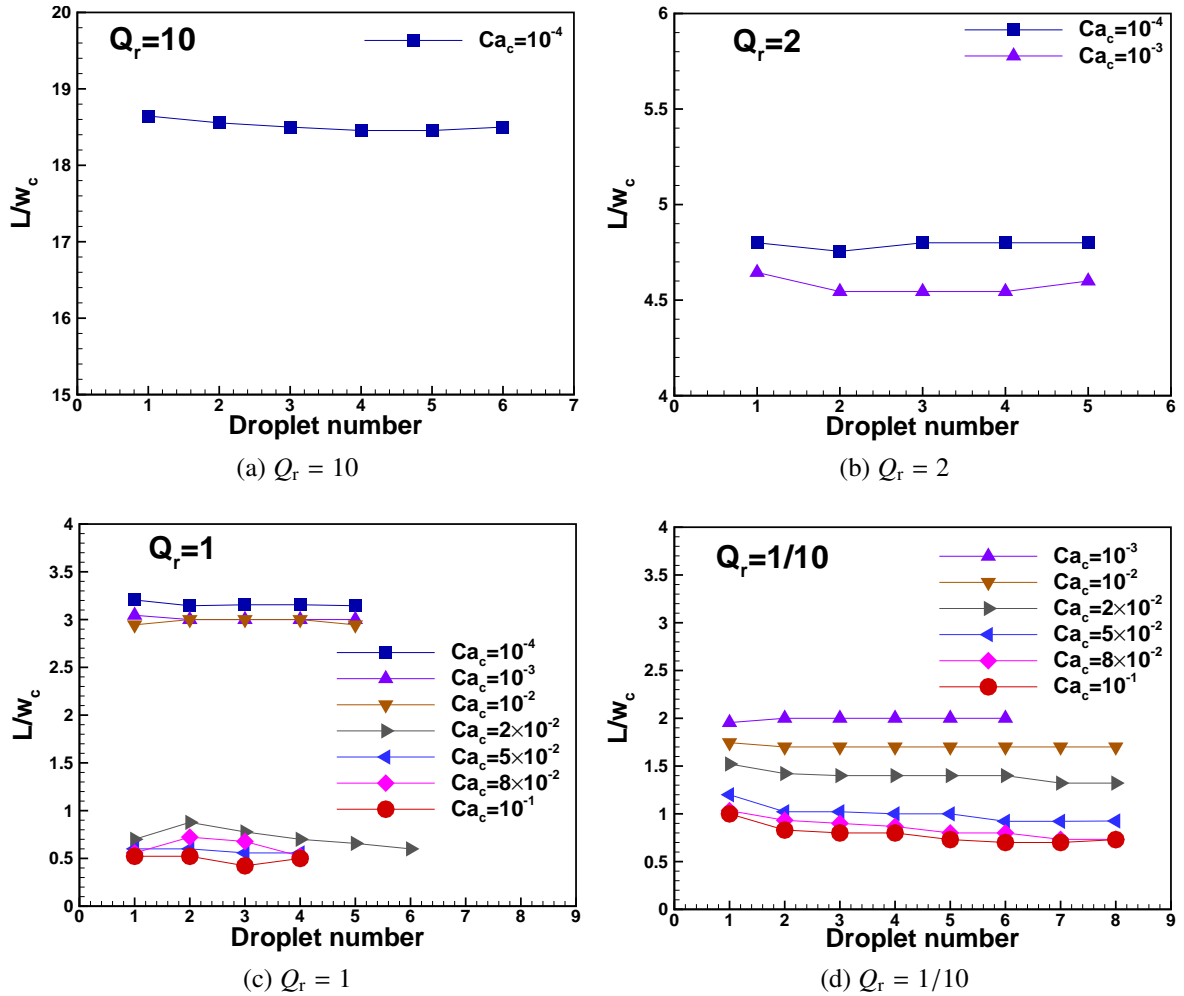


Figure 6: Dependence of droplet length (L/w_c) on Ca_c .

in Figure 6c. As Ca_c is further increased, the flow is transiting into another regime at $Ca_c = 2 \times 10^{-2}$. It is denoted as a critical or transitional capillary number ($Ca_{c,trans}$) for the continuous phase. For $Q_r < 1$, the critical capillary number ($Ca_{c,trans}$) increases up to $Q_r = 1/2$. For sufficiently low values of $Q_r (< 1/2)$, $Ca_{c,trans}$ becomes constant.

Further, the combined influences of viscosity and flow rate on the droplet length are analyzed by plotting the length of each droplet as a function of Q_r in Figure 7 at a fixed Ca_c . For a given Ca_c and Q_r , it is observed that the droplets being formed are of the same length and mono-dispersed. However, the droplet length is decreasing with Q_r , under otherwise identical conditions. This observation remains valid for a wide range of Ca_c and Q_r , as shown in Figure 7. Nevertheless, the curves corresponding to $Q_r \geq 1$ in Figures 7c and 7d show a different trend, as discussed previously. The downstream region fills with the droplets after an initial transient in the

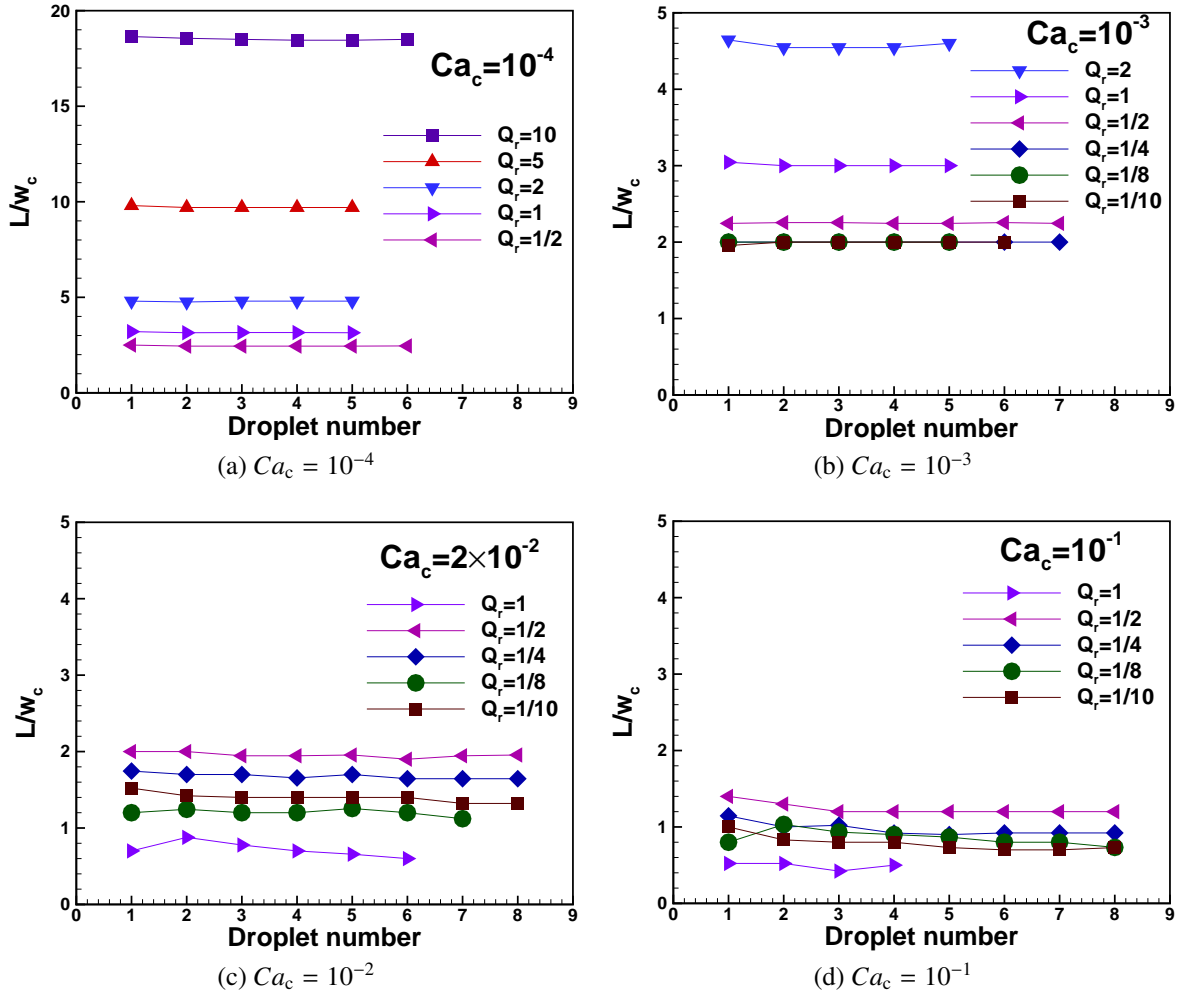


Figure 7: Dependence of droplet length (L/w_c) on Q_r .

hydrodynamic development of two-phase flow. Hence, the droplet length is calculated as an average only after the downstream channel is completely filled. Further, the non-repeatability of exact necking instability leading to the formation of droplets results in the droplets length variation of about 2 – 5% in the dripping regime. It can also be observed from Figure 7 about the droplet length varying initially and reaching a steady yet insignificant oscillatory behavior. The numerical data of the droplet length (L/w_c) in the ‘squeezing regime’ is statistically represented by the following empirical linear relation.

$$L = (\alpha + \beta Q_r)w_c \quad (\text{squeezing regime}) \quad (12)$$

where $\alpha = 1$ and $\beta = 1.7648$ for all values of Q_r .

The empirical correlation (Eq. 12) suggests that the droplet length (L) is mainly dependent on the flow rate ratio (Q_r), and the size of the channel (w_c) whereas independent of the physical properties like viscosity (μ) and interfacial tension (σ). Similar empirical correlations are reported for other geometrical arrangements by several experimental and numerical studies (Garstecki et al., 2006; De menez et al., 2008; Bashir et al., 2011; Nekouei and Vanapalli, 2017).

Further, the numerical data for the droplet length (L/w_c) in the ‘dripping regime’ is represented statistically by the following empirical power-law relation.

$$L = (\alpha Q_r^\beta Ca_c^\gamma)w_c \quad (\text{dripping regime}) \quad (13)$$

where $\alpha = 0.5358$, $\beta = 0.2307$ and $\gamma = -0.3682$ for $Ca_c > 10^{-2}$.

The droplet length in the dripping regime depends in a non-linear manner on the capillary number, flow rate, and channel dimensions. This relation (Eq. 13) is qualitatively consistent with the literature (Christopher et al., 2008; Xu et al., 2008; Gupta and Kumar, 2010; Zhang et al., 2018) for other geometrical arrangements.

A parity plot (Figures 8a and 8b) shows excellent comparison ($R^2 = 0.9899$) of the present numerical data and predictions of empirical relation (Eqs. 12 and 13) for the droplet length (L/w_c) in the squeezing and dripping regimes.

4.5. Droplet detachment time

The dimensionless detachment time of the droplet is defined as $\tau_{dd} = (u_c t_{dd}/w_c)$, where u_c is the velocity of the continuous phase and t_{dd} (Eq. 8) is detachment time of droplet. Figures 9 and 10 illustrate the variation of the droplet detachment time (τ_{dd}) with Ca_c and Q_r under the droplet formation regimes (Eq. 11). To explore the effect of interfacial tension on the droplet generation, Figure 9 shows variation of τ_{dd} (time interval between generation of two subsequent droplets) with Ca_c for the fixed Q_r . In general, the droplets detachment time (τ_{dd}) increases with decreasing Ca_c for fixed Q_r . It is observed that the time taken for the formation (τ_{dd}) of the first droplet is either more or equal than the subsequent droplets due to the hydrodynamic development in the main channel, depending on the values of Ca_c and Q_r .

Under the squeezing regime ($Q_r > 1$ and $Ca_c < 10^{-2}$), τ_{dd} is almost equal for all, including the first, droplets at very high Q_r , see Figure 9a, whereas as Q_r decreased, τ_{dd} for first droplets is greater than that for all other subsequent droplets formed at approximately constant τ_{dd} , see Figure 9b. For $Q_r = 1$, τ_{dd} is decreasing with increasing Ca_c till the formation of the few droplets and showing some fluctuations in the initial stage because both phases are flowing with the same flow rates having equal viscosity and density, as shown in Figure 9c. For $Q_r > 1$, τ_{dd} is decreasing smoothly and reaching steady for all the values of Ca_c , as shown in Figure 9d.

Further, to explore the effect of relative flow rates of the two-phases on the droplet generation, Figure 10 shows the droplet formation time (τ_{dd}) of each droplet as a function of Q_r for the fixed

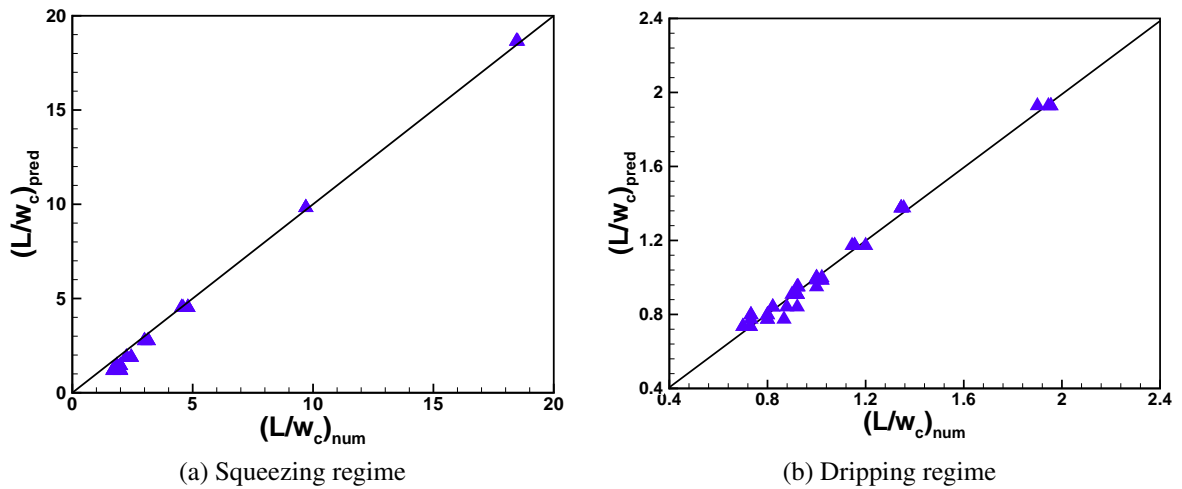


Figure 8: Parity plots between numerical and predicted (Eqs. 12 and 13) values of droplet length (L/w_c).

Ca_c . Here also τ_{dd} is decreasing with a decrease in Q_r for a fixed Ca_c . The τ_{dd} is smoothly decreasing and becoming constant after the formation of a few droplets. It implies that both viscosity and interfacial tension have qualitatively similar influences on the droplet formation time (τ_{dd}) in the droplet zone, i.e., squeezing and dripping flow regimes. The droplet detachment time (τ_{dd}) shows a complex dependence on Q_r and Ca_c . Such behaviour of τ_{dd} is qualitatively consistent with the previous studies (Husny and Cooper-White, 2006; Nazari et al., 2018) for varied geometrical arrangements of the microfluidic devices. In particular, a smaller value of τ_{dd} is favorable to produce mono-dispersed droplets of uniform size. It is further analyzed in the subsequent section in terms of the frequency of the droplet generation.

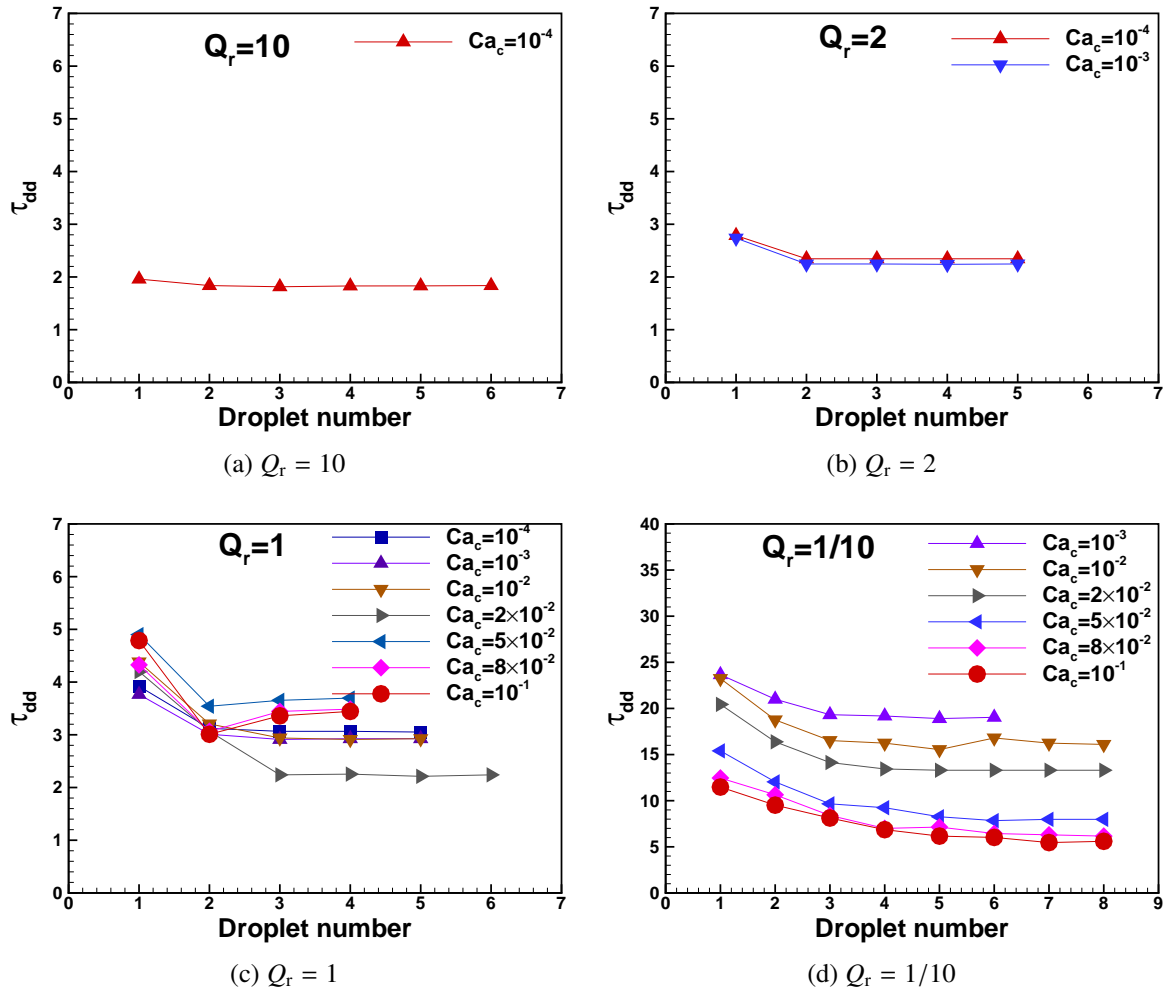


Figure 9: Droplet detachment time (τ_{dd}) as a function of Ca_c for fixed Q_r .

4.6. Droplet generation frequency

The dimensionless droplet generation frequency ($\bar{f}_{dd} = 1/\tau_{dd}$, Eq. 8) is calculated as the inverse of the detachment time of the droplet (τ_{dd} , Figures 9 and 10). The dependence of \bar{f}_{dd} on Q_r and Ca_c under the droplet zone is shown in Figure 11. When the flow rates of both the continuous and dispersed phases are equal (i.e., $Q_r = 1$), \bar{f}_{dd} remains almost constant in the squeezing regime for the lower values of Ca_c ($< 10^{-2}$). There is, however, a sudden jump in \bar{f}_{dd} at $Ca_c = 2 \times 10^{-2}$ and it is decreasing beyond $Ca_c > 10^{-2}$, as seen in Figure 11a. In the case of $Q_r = 1$ in the present study, the viscosities of both phases are equal. Therefore, the flow patterns transit into the parallel regime after forming few droplets with increasing Ca_c . The shear stress exerted by the continuous fluid on the dispersed phase interface is insufficient to overcome the interfacial forces to create a droplet. Whereas for $Q_r = 1/2$, the frequency \bar{f}_{dd} increases with the increase Ca_c and attaining a

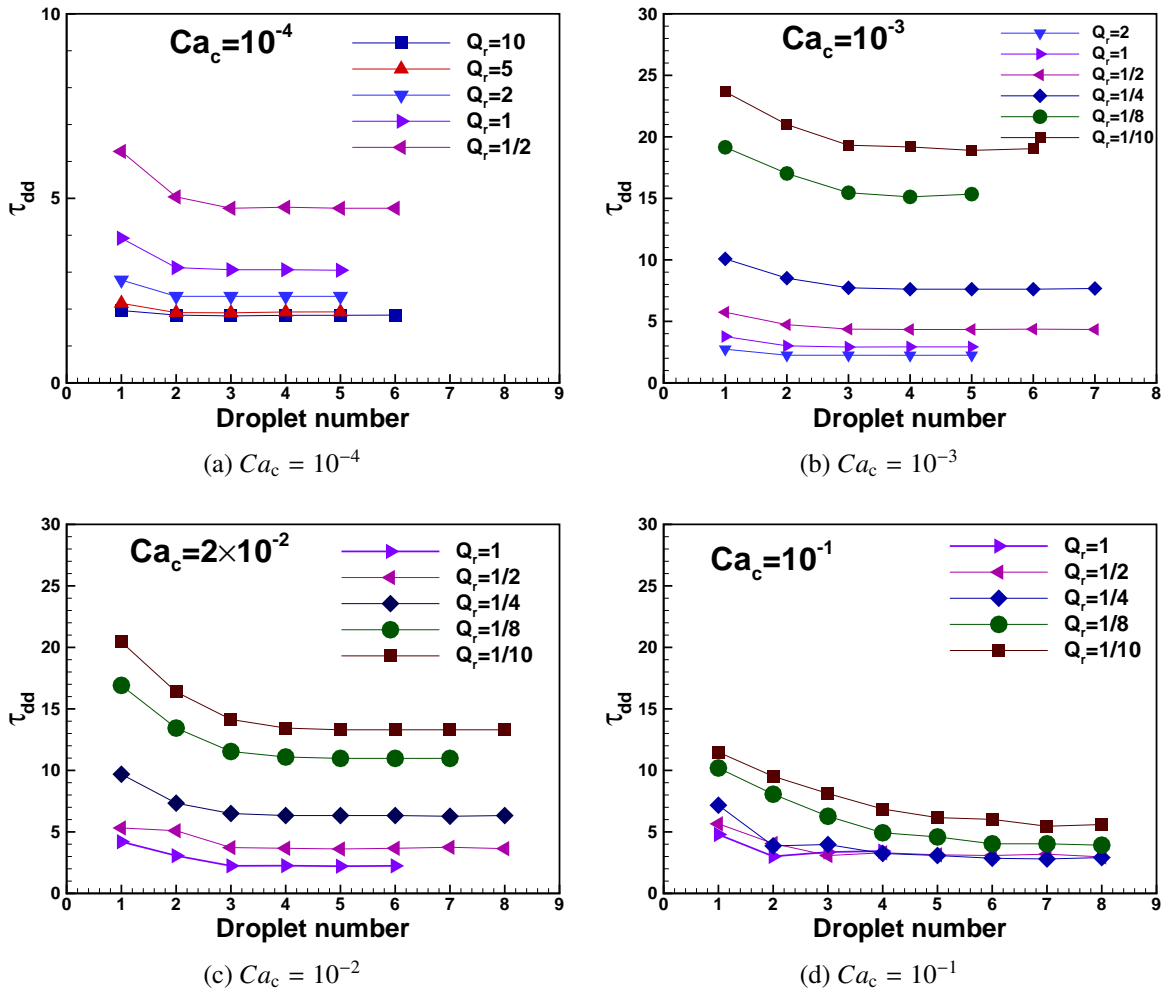


Figure 10: Droplet detachment time (τ_{dd}) as a function of Q_r for fixed Ca_c .

maximum value at $Ca_c = 5 \times 10^{-2}$, and it decreases sharply thereafter. Such a complex dependence of \bar{f}_{dd} on Q_r and Ca_c is attributed to the significantly larger elongated droplets ($L \gg w_c$) observed under the squeezing and first transitional flow regimes.

In contrast to nature of \bar{f}_{dd} seen in Figure 11a, the behaviour of \bar{f}_{dd} is, however, quite different in Figures 11b and 11c under the dripping regime. In general, the frequency of droplet generation proportionally enhances, i.e., an increasing number of droplets per unit time, with both increasing Q_r and Ca_c , as displayed by Figures 11b and 11c. The present droplet frequency results are consistent with previous experimental and numerical studies (Christopher et al., 2008; Gupta and Kumar, 2010) for varied geometrical arrangements.

The influence of interfacial tension ($Ca_c \geq 10^{-2}$) on the droplet generation frequency (\bar{f}_{dd}) is depicted in Figure 11b for the fixed Q_r . The numerical data presented in Figure 11b has shown the

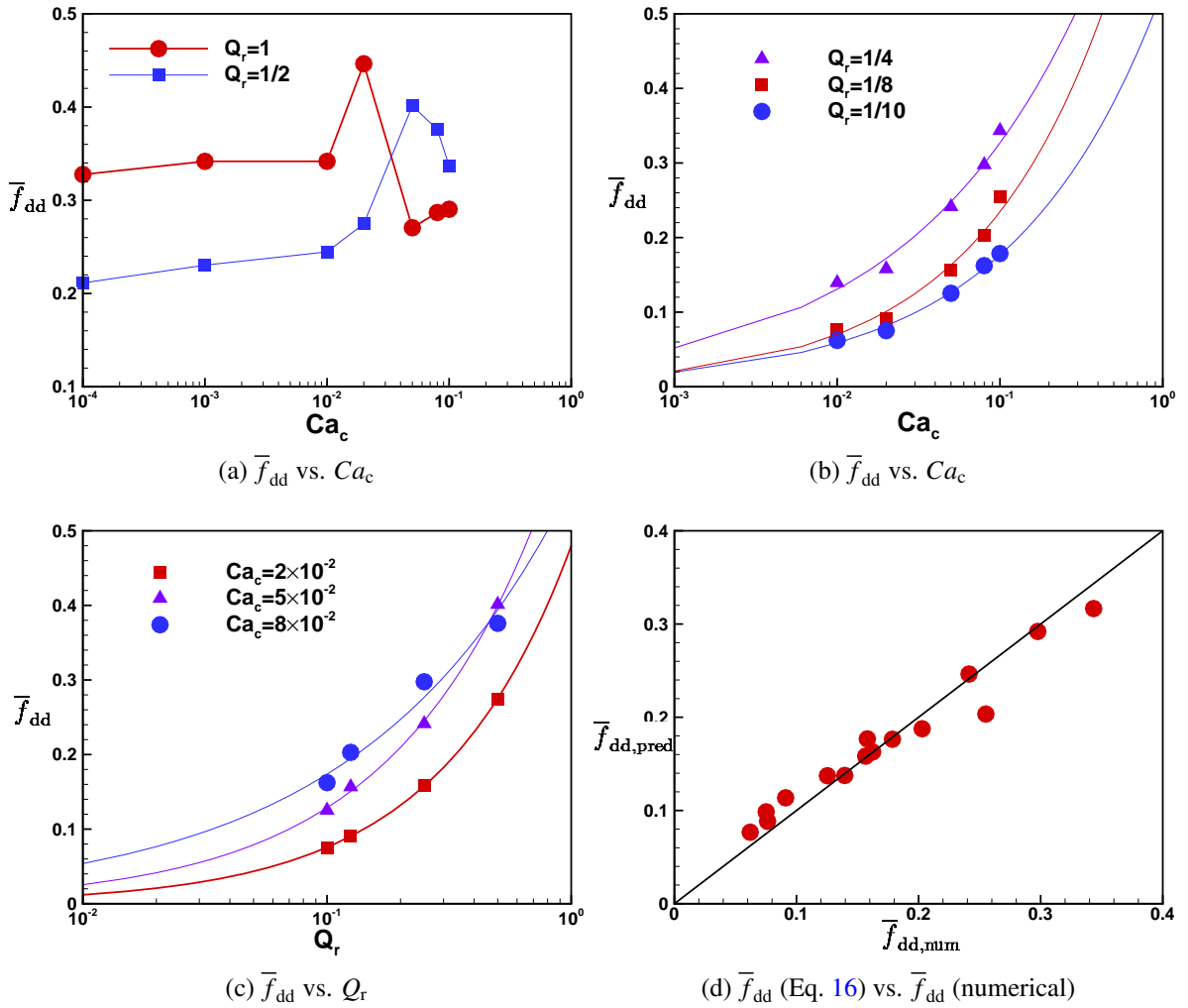


Figure 11: Dependence of droplet frequency on Ca_c and Q_r .

power-law dependence of \bar{f}_{dd} on Ca_c for the fixed Q_r as follows.

$$\bar{f}_{dd} = \alpha Ca_c^\beta \quad (14)$$

The values of the statistical constants (α and β) are shown in Table 3a for the ranges of conditions ($1/10 \leq Q_r \leq 1/4$, and $10^{-2} \leq Ca_c \leq 10^{-1}$) of dripping flow regime.

Further, Figure 11c depicts the influence of flow rates ratio (Q_r) on the droplet generation frequency (\bar{f}_{dd}) for the fixed Ca_c . A statistical analysis of the numerical data presented in Figure 11c has also shown the power-law dependence of \bar{f}_{dd} on Q_r for the fixed Ca_c as follow.

$$\bar{f}_{dd} = \alpha Q_r^\beta \quad (15)$$

The values of the statistical constants (α and β) are shown in Table 3b for the ranges of conditions ($1/10 \leq Q_r \leq 1/4$; $10^{-2} \leq Ca_c \leq 10^{-1}$) of dripping flow regime.

Furthermore, to determine the combined influences of interfacial, inertial and viscous forces, a new correlation is proposed to predict the functional dependence of \bar{f}_{dd} on Q_r and Ca_c under the dripping flow regime ($1/10 \leq Q_r \leq 1/2$ and $10^{-2} \leq Ca_c \leq 0.1$) as follows.

$$\bar{f}_{dd} = \alpha Q_r^\beta Ca_c^\gamma \quad (16)$$

where $\alpha = 2.3$, $\beta = 0.417$ and $\gamma = 0.685$ with the coefficient of determination $R^2 = 0.9634$. A parity plot in Figure 11d displays an excellent agreement between the present numerical and predicted (using Eq. 16) values of droplet generation frequency (\bar{f}_{dd}).

Table 3: Statistical analysis for dependence of \bar{f}_{dd} on Ca_c and Q_r .

(a) $\bar{f}_{dd} = \alpha Ca_c^\beta$				(b) $\bar{f}_{dd} = \alpha Q_r^\beta$			
$10Q_r$	α	β	R^2	$10^2 Ca_c$	α	β	R^2
2.50	0.8202	0.3994	0.9758	2	0.4799	0.8022	0.9990
1.25	0.7856	0.5249	0.9746	5	0.6511	0.7041	0.9968
1.00	0.5321	0.4791	0.9874	8	0.5607	0.5091	0.9677

5. Conclusions

The microfluidic phenomena of droplet formation in a two-dimensional cross-flow T-junction geometry have been studied numerically for a wide range of conditions ($Re_c = 0.1$, $10^{-4} \leq Ca_c \leq 1$, $0.1 \leq Q_r \leq 10$, $\rho_r = 1$ and $w_r = 1$) by using the conservative level set method in conjunction with the finite element modelling approach. In-depth insights into droplet generation and dynamics are presented in terms of instantaneous phase (ϕ) profiles, dimensionless droplet size (L/w_c), detachment time (τ_{dd}), and frequency (\bar{f}_{dd}) as a function of flow governing parameters (Ca_c and Q_r). Evidently, even at $Ca_c > 10^{-2}$ where the interfacial force dominates the pressure build-up in the upstream region is responsible for the droplet generation. The two-phase microfluidic flow is characterized as squeezing, the first transition, dripping, second transition, parallel, and jet-type flow regimes based on the nature of flow as droplets of elongated or circular shape, slug, and parallel layers. A transitional capillary number ($Ca_{r,trans}$) is defined to express the changes in the droplet shape from a regular mono-dispersed to an irregular poly-dispersed. Interestingly, the ratio of transition capillary numbers of continuous and dispersed phases varied proportionally as a quadratic function of their flow rate ratio, $Ca_{r,trans} = \beta Q_r^2$. This splits $Ca_{r,trans}$ versus Q_r plane into two zones: (i) droplet zone ($Ca_{r,trans} > \beta Q_r^2$), and (ii) non-droplet zone ($Ca_{r,trans} < \beta Q_r^2$). The droplet zone comprises of the squeezing, first transition, and dripping flow regimes. On the other hand, the second transition, parallel and jet-type flow regimes fall under the non-droplet zone. This classification helps to predict the possibility of the droplet formation for a particular Ca_c and Q_r . The droplet dynamics have also shown the complex dependence on the governing parameters (Ca_c and Q_r). The droplet length is linearly dependent on Q_r in the squeezing flow regime, whereas power-law dependence on Ca_c and Q_r in the dripping flow regime. A new correlation has been proposed to predict the dimensionless frequency of the droplet generation in the dripping flow regime as a power-law function of Ca_c and Q_r . The present results have been verified and shown excellent correspondence with the limited experimental and numerical studies available in the literature. Finally, the presented flow regimes and predictive correlations guide their use in the engineering and design of microfluidic droplet generators.

Declaration of Competing Interest

All authors declare that they have no conflict of interest. The authors certify that they have NO affiliations with or involvement in any organization or entity with any financial interest (such as honoraria; educational grants; participation in speakers' bureaus; membership, employment, consultancies, stock ownership, or other equity interest; and expert testimony or patent-licensing arrangements), or non-financial interest (such as personal or professional relationships, affiliations, knowledge or beliefs) in the subject matter or materials discussed in this manuscript.

Acknowledgements

R.P. Bharti would like to acknowledge Science and Engineering Research Board (SERB), Department of Science and Technology (DST), Government of India (GoI) for providence of MATRICS grant (File No. MTR/2019/001598).

Nomenclature

Ca_c	capillary number for CP (Eq. 9), dimensionless
$Ca_{c,trans}$	transitional or threshold capillary number for CP (Eq. 11), dimensionless
Ca_d	capillary number for DP (Eq. 9), dimensionless
$Ca_{d,trans}$	transitional capillary number for DP (Eq. 11), dimensionless
Ca_r	ratio of capillary numbers (Eq. 10), dimensionless
$Ca_{r,trans}$	ratio of transitional capillary numbers (Eq. 11), dimensionless
d_{eff}	effective droplet diameter (Eq. 7), m
\mathbf{D}	rate of strain tensor (Eq. 3), s^{-1}
f_{dd}	droplet detachment frequency, s^{-1}
\mathbf{F}_σ	interfacial force (Eq. 5), N
L_d	downstream length of the main channel, m
L_m	length of the main channel, m
L_s	length of the side channel, m
L_u	upstream length of the main channel, m
p	pressure, Pa

Q_c	flow rate of CP, m ³ /s
Q_d	flow rate of DP, m ³ /s
Q_r	flow rate ratio (Eq. 10), dimensionless
Re_c	Reynolds number for CP (Eq. 9), dimensionless
Re_d	Reynolds number for DP (Eq. 9), dimensionless
Re_r	ratio of Reynolds numbers (Eq. 10), dimensionless
t_{dd}	droplet detachment time, s
\mathbf{u}	velocity vector, m/s
w_c	width of the main channel, m
w_d	width of the side channel, m
w_r	channel width ratio (Eq. 10), dimensionless
x	stream-wise coordinate
y	transverse coordinate

Dimensionless groups

Ca	Capillary number (Eq. 9), dimensionless
Re	Reynolds number (Eq. 9), dimensionless

Greek letters

ϵ_{is}	interface thickness controlling parameter (Eq. 6), m
γ	re-initialization or stabilization parameter (Eq. 6), m/s
κ	curvature of the interface, m
μ_c	viscosity of CP, Pa.s
μ_d	viscosity of DP, Pa.s
μ_r	viscosity ratio (Eq. 10), dimensionless
ϕ	level set function, dimensionless
ρ_c	density of CP, kg/m ³
ρ_d	density of DP, kg/m ³
ρ_r	density ratio (Eq. 10), dimensionless
σ	interfacial tension, N/m
τ	extra stress tensor (Eq. 3), N/m ²
τ_{dd}	droplet detachment time, dimensionless
θ	contact angle, degrees

Abbreviations

BDF	backward differentiation formula
CFD	computational fluid dynamics
CP	continuous phase
DAE	differential algebraic equations
DP	disperse phase
FDM	finite difference method
FEM	finite element method
FVM	finite volume method
LBM	lattice Boltzmann method
LSM	level set method
PARDISO	parallel direct solver
PFM	phase field method
VOF	volume of fluid

References

- Abate, A. R., Mary, P., Van Steijn, V., Weitz, D. A., 2012. Experimental validation of plugging during drop formation in a T-junction. *Lab on a Chip* 12, 1516–1521.
- Akhlaghi Amiri, H. A., Hamouda, A. A., 2013. Evaluation of level set and phase field methods in modeling two phase flow with viscosity contrast through dual-permeability porous medium. *International Journal of Multiphase Flow* 52, 22–34.
- Anna, S. L., 2016. Droplets and Bubbles in Microfluidic Devices. *Annual Review of Fluid Mechanics* 48, 285–309.
- Anna, S. L., Bontoux, N., Stone, H. A., 2003. Formation of dispersions using "flow focusing" in microchannels. *Applied Physics Letters* 82, 364–366.
- Asua, J., 2002. Miniemulsion polymerization. *Progress in Polymer Science* 27, 1283–1346.
- Barnes, H. A., 1994. Rheology of emulsions - a review. *Colloids and Surfaces A: Physicochemical and Engineering Aspects* 91, 89–95.
- Bashir, S., Rees, J. M., Zimmerman, W. B., 2011. Simulations of microfluidic droplet formation using the two-phase level set method. *Chemical Engineering Science* 66, 4733–4741.
- Bashir, S., Rees, J. M., Zimmerman, W. B., 2014. Investigation of pressure profile evolution during confined microdroplet formation using a two-phase level set method. *International Journal of Multiphase Flow* 60, 40–49.
- Bharti, R. P., Chhabra, R. P., Eswaran, V., 2006. Steady flow of power law fluids across a circular cylinder. *Canadian Journal of Chemical Engineering* 84 (4), 406–421.

- Bharti, R. P., Chhabra, R. P., Eswaran, V., 2007a. Two-dimensional steady poiseuille flow of power-law fluids across a circular cylinder in a plane confined channel: wall effects and drag coefficient. *Industrial & Engineering Chemistry Research* 46 (11), 3820–3840.
- Bharti, R. P., Chhabra, R. P., Eswaran, V., 2007b. Effect of blockage on heat transfer from a cylinder to power law liquids. *Chemical Engineering Science* 62 (17), 4729–4741.
- Bollhöfer, M., Schenk, O., Janalik, R., Hamm, S., Gullapalli, K., 2020. State-of-the-art sparse direct solvers. In: Grama, A., Sameh, A. (Eds.), *Parallel Algorithms in Computational Science and Engineering*. Birkhäuser, Cham, Boston, MA, Ch. 1, pp. 3 – 33.
- Christopher, G. F., Noharuddin, N. N., Taylor, J. A., Anna, S. L., 2008. Experimental observations of the squeezing-to-dripping transition in T-shaped microfluidic junctions. *Physical Review E* 78, 036317.
- Cristini, V., Tan, Y. C., 2004. Theory and numerical simulation of droplet dynamics in complex flows - A review. *Lab on a Chip* 4, 257–264.
- De mencech, M., Garstecki, P., Jousse, F., Stone, H. A., 2008. Transition from squeezing to dripping in a microfluidic T-shaped junction. *Journal of Fluid Mechanics* 595, 141–161.
- Doufène, K., Tourné-Péteilh, C., Etienne, P., Aubert-Pouëssel, A., 2019. Microfluidic systems for droplet generation in aqueous continuous phases: A focus review. *Langmuir* 35 (39), 12597–12612.
- Eggers, J., Villermaux, E., 2008. Physics of liquid jets. *Reports on Progress in Physics* 71 (3), 036601.
- Gangawane, K. M., Bharti, R. P., 2018. Computational analysis of mhd natural convection in partially-differentially heated cavity: effect of cooler size. *IMEchE, Part C: Journal of Mechanical Engineering Science* 232, 515–528.
- Garstecki, P., Fuerstman, M. J., Stone, H. A., Whitesides, G. M., 2006. Formation of droplets and bubbles in a microfluidic T-junction - Scaling and mechanism of break-up. *Lab on a Chip* 6 (3), 437–446.
- Gerecsei, T., Ungai-Salanki, R., Saftics, A., Derényi, I., Horvath, R., Szabo, B., 2020. Characterization of the dissolution of water microdroplets in oil. [arXiv:2003.12494](https://arxiv.org/abs/2003.12494).
- Glawdel, T., Elbuken, C., Ren, C. L., Jan 2012a. Droplet formation in microfluidic T-junction generators operating in the transitional regime. I. Experimental observations. *Physical Review E* 85, 016322.
- Glawdel, T., Elbuken, C., Ren, C. L., 2012b. Droplet formation in microfluidic T-junction generators operating in the transitional regime. II. Modeling. *Physical Review E* 85, 016323.
- Glawdel, T., Elbuken, C., Ren, C. L., 2013. *Droplet Generation in Microfluidics*. Springer US, Boston, MA, pp. 1–12.
- Glawdel, T., Ren, C. L., 2012. Droplet formation in microfluidic T-junction generators operating in the transitional regime. III. Dynamic surfactant effects. *Physical Review E* 86, 026308.
- Gupta, A., Kumar, R., 2010. Flow regime transition at high capillary numbers in a microfluidic T-junction: Viscosity contrast and geometry effect. *Physics of Fluids* 22, 122001.
- Husny, J., Cooper-White, J. J., 2006. The effect of elasticity on drop creation in T-shaped microchannels. *Journal of Non-Newtonian Fluid Mechanics* 137, 121–136.
- Jamalabadi, M. Y. A., DaqiqShirazi, M., Kosar, A., Shadloo, M. S., 2017. Effect of injection angle, density ratio, and

- viscosity on droplet formation in a microfluidic T-junction. *Theoretical and Applied Mechanics Letters* 7, 243–251.
- Kang, K.-K., Lee, B., Lee, C.-S., 2019. Recent progress in the synthesis of inorganic particulate materials using microfluidics. *Journal of the Taiwan Institute of Chemical Engineers* 98, 2–19.
- Kumar, R., Lal, A. K., Bharti, R. P., Pancholi, V., 2021. Experimental and computational analysis of material flow characteristics in friction stir welding. *International Journal of Advanced Manufacturing Technology* 115, 3011–3020.
- Li, X., He, L., He, Y., Gu, H., Liu, M., 2019. Numerical study of droplet formation in the ordinary and modified T-junctions. *Physics of Fluids* 31, 082101.
- Li, X. B., Li, F. C., Yang, J. C., Kinoshita, H., Oishi, M., Oshima, M., 2012. Study on the mechanism of droplet formation in T-junction microchannel. *Chemical Engineering Science* 69, 340–351.
- Liu, C., Zhu, C., Fu, T., Ma, Y., Li, H. Z., 2019. Interfacial dynamics of the core-annular flow for glycerol–water solution / ionic liquid ([BMIM][PF6]) two-phase flow in a microfluidic flow-focusing junction. *Journal of the Taiwan Institute of Chemical Engineers* 98, 45–52.
- Liu, H., Zhang, Y., 2009. Droplet formation in a T-shaped microfluidic junction. *Journal of Applied Physics* 106, 034906.
- Liu, H., Zhang, Y., 2011. Lattice Boltzmann simulation of droplet generation in a microfluidic cross-junction. *Communications in Computational Physics* 9, 1235–1256.
- Mansard, V., Mecca, J. M., Dermody, D. L., Malotky, D., Tucker, C. J., Squires, T. M., 2016. Collective Rayleigh-Plateau Instability: A Mimic of Droplet Breakup in High Internal Phase Emulsion. *Langmuir* 32, 2549–2555.
- Mulqueen, P., 2003. Recent advances in agrochemical formulation. *Advances in Colloid and Interface Science* 106, 83–107.
- Nazari, M., Sani, H. M., Kayhani, M. H., Daghighi, Y., 2018. Different stages of liquid film growth in a microchannel: Two-phase lattice boltzmann study. *Brazilian Journal of Chemical Engineering* 35, 977–994.
- Nekouei, M., Vanapalli, S. A., 2017. Volume-of-fluid simulations in microfluidic T-junction devices: Influence of viscosity ratio on droplet size. *Physics of Fluids* 29, 032007.
- Nisisako, T., Torii, T., Higuchi, T., 2002. Droplet formation in a microchannel network. *Lab on a Chip* 2, 24–26.
- Olsson, E., Kreiss, G., 2005. A conservative level set method for two phase flow. *Journal of Computational Physics* 210, 225–246.
- Osher, S., Sethian, J. A., 1988. Fronts propagating with curvature-dependent speed: Algorithms based on Hamilton-Jacobi formulations. *Journal of Computational Physics* 79, 12–49.
- Patnana, V. K., Bharti, R. P., Chhabra, R. P., 2009. Two dimensional unsteady flow of power-law fluids over a cylinder. *Chemical Engineering Science* 64 (12), 2978–2999.
- Patnana, V. K., Bharti, R. P., Chhabra, R. P., 2010. Two dimensional unsteady forced convection heat transfer in power-law fluids from a heated cylinder. *International Journal of Heat and Mass Transfer* 53 (19-20), 4152–4167.
- Ram, R. P., Bharti, R. P., Dhiman, A. K., 2016. Forced convection flow and heat transfer across an in-line bank of

- circular cylinders. *Canadian Journal of Chemical Engineering* 94, 1381–1385.
- Sartipzadeh, O., Naghib, S. M., Seyfoori, A., Rahmanian, M., Fateminia, F. S., 2020. Controllable size and form of droplets in microfluidic-assisted devices: Effects of channel geometry and fluid velocity on droplet size. *Materials Science and Engineering: C* 109, 110606.
- Schenk, O., Gärtner, K., 2011. PARDISO. In: Padua, D. (Ed.), *Encyclopedia of Parallel Computing*. Springer US, Boston, MA, pp. 1458–1464.
- Shi, Y., Tang, G. H., Xia, H. H., 2014. Lattice Boltzmann simulation of droplet formation in T-junction and flow focusing devices. *Computers and Fluids* 90, 155–163.
- Sivakumar, P., Bharti, R. P., Chhabra, R. P., 2006. Effect of power-law index on critical parameters for power-law flow across an unconfined circular cylinder. *Chemical Engineering Science* 61 (18), 6035–6046.
- Soh, G. Y., Yeoh, G. H., Timchenko, V., 2016. Numerical investigation on the velocity fields during droplet formation in a microfluidic T-junction. *Chemical Engineering Science* 139, 99–108.
- Stone, H., Stroock, A., Ajdari, A., 2004. Engineering Flows in Small Devices. *Annual Review of Fluid Mechanics* 36, 381–411.
- Tarchichi, N., Chollet, F., Manceau, J. F., 2013. New regime of droplet generation in a T-shape microfluidic junction. *Microfluidics and Nanofluidics* 14, 45–51.
- Thorsen, T., Roberts, R. W., Arnold, F. H., Quake, S. R., 2001. Dynamic pattern formation in a vesicle-generating microfluidic device. *Physical Review Letters* 86, 4163–4166.
- Tian, F. B., Bharti, R. P., Xu, Y. Q., 2014. Deforming-spatial-domain/stabilized space–time (DSD/SST) method in computation of non-newtonian fluid flow and heat transfer with moving boundaries. *Computational Mechanics* 53 (2), 257–271.
- van der Graaf, S., Nisisako, T., G. P. H. Schroën, C., G. M. van der Sman, R., M. Boom, R., 2006. Lattice Boltzmann Simulations of Droplet Formation in a T-Shaped Microchannel. *Langmuir* 22, 4144–4152.
- van der Schaaf, U. S., 2017. Emulsions. In: *Ullmann’s Encyclopedia of Industrial Chemistry*. pp. 1–15.
- Van Steijn, V., Kleijn, C. R., Kreutzer, M. T., 2010. Predictive model for the size of bubbles and droplets created in microfluidic T-junctions. *Lab on a Chip* 10, 2513–2518.
- Vishal, G., Tomar, J., Bharti, R. P., 2021. Critical parameters for non-newtonian shear-thickening power-law fluids flow across a channel confined circular cylinder. *Journal of the Taiwan Institute of Chemical Engineers* 123, 34–46.
- Wehking, J. D., Gabany, M., Chew, L., Kumar, R., 2014. Effects of viscosity, interfacial tension, and flow geometry on droplet formation in a microfluidic T-junction. *Microfluidics and Nanofluidics* 16, 441–453.
- Whitesides, G. M., 2006. The origins and the future of microfluidics. *Nature* 442, 368–373.
- Wong, V. L., Loizou, K., Lau, P. L., Graham, R. S., Hewakandamby, B. N., 2017. Numerical studies of shear-thinning droplet formation in a microfluidic T-junction using two-phase level-SET method. *Chemical Engineering Science* 174, 157–173.
- Wong, V. L., Loizou, K., Lau, P. L., Graham, R. S., Hewakandamby, B. N., 2019. Characterizing droplet breakup rates

- of shear-thinning dispersed phase in microreactors. *Chemical Engineering Research and Design* 144, 370–385.
- Xu, J. H., Li, S. W., Tan, J., Luo, G. S., 2008. Correlations of droplet formation in T-junction microfluidic devices: From squeezing to dripping. *Microfluidics and Nanofluidics* 5, 711–717.
- Yu, W., Liu, X., Zhao, Y., Chen, Y., 2019. Droplet generation hydrodynamics in the microfluidic cross-junction with different junction angles. *Chemical Engineering Science* 203, 259 – 284.
- Zeng, W., Fu, H., 2020. Measurement of fluid viscosity based on droplet microfluidics. *Physics of Fluids* 32, 042002.
- Zhang, Q., Zhu, C., Du, W., Liu, C., Fu, T., Ma, Y., Li, H. Z., 2018. Formation dynamics of elastic droplets in a microfluidic T-junction. *Chemical Engineering Research and Design* 139, 188–196.
- Zhu, P., Wang, L., 2017. Passive and active droplet generation with microfluidics: a review. *Lab on a Chip* 17, 34–75.